Transient Stability Analysis and Coordinated Control Strategy of DC-link Voltage for PLL-based Grid-connected DFIG System During Asymmetrical Grid Faults

Yi Luo, Jun Yao, *Member*, *IEEE*, Dong Yang, Hai Xie, Linsheng Zhao, and Rongyu Jin

***Abstract*—The transient behavior of DC-link voltage (DCV) significantly affects the low-voltage ride-through for phase-locked loop (PLL)-based grid-connected doubly-fed induction generator (DFIG) systems. This study investigates the DCV transient behavior of a PLL-based DFIG system under asymmetrical grid faults. First, by considering the coupling characteristics of positive and negative sequence (PNS) components, a nonlinear large-signal model of DCV is developed. Furthermore, the transient characteristics of DCV under varying parameters are analyzed using phase trajectory diagrams. In addition, the transient stability (TS) mechanism of DCV during asymmetrical faults is examined through an energy function approach. The analysis indicates that the transient instability of DCV is primarily associated with the control characteristics of PNS PLLs, while the TS level of DCV is mainly determined by the power coordination control between the rotor side converter and grid side converter. Moreover, a coordinated control strategy is proposed to enhance the TS of DCV under asymmetrical grid faults. Finally, both simulation and experimental results are presented to validate the theoretical analysis and the effectiveness of the proposed strategy.**

***Index Terms*—Transient stability, DC-link voltage, doubly-fed induction generator, asymmetrical grid faults, stability control strategy.**

Received: March 23, 2025
Accepted: November 1, 2025
Published Online: January 1, 2026
Yi Luo, Jao Yao (corresponding author), Dong Yang, Hai Xie, Linsheng Zhao, and Rongyu Jin are with the State Key Laboratory of Power Transmission Equipment Technology, School of Electrical Engineering, Chongqing University, Chongqing 400044, China (e-mail: 20211101021@cqu.edu.cn; jyao@cqu.edu.cn; 202211131100t@stu.cqu.edu.cn; 202211131293@stu.cqu.edu.cn; zls410@stu.cqu.edu.cn; jry2001@cqu. edu.cn).
DOI: 10.23919/PCMP.2024.000345

NOMENCLATURE

A. Abbreviations

PLL	phase-locked loop
DFIG	doubly-fed induction generator
DCV	DC-link voltage
RSC	rotor side converter
GSC	grid side converter
REPF	renewable energy power farm
PS	positive sequence
NS	negative sequence

B. Variables

$\boldsymbol{U}_{\mathrm{f}}$	vectors of faulted grid voltage
$\boldsymbol{U}_{\mathrm{s}}$	stator voltage
$\boldsymbol{I}$	output current of DFIG
$R_{\mathrm{s}}, L_{\mathrm{s}}$	stator resistance and inductance
$R_{\mathrm{r}}, L_{\mathrm{r}}$	rotor resistance and inductance
L_{m}	mutual inductance
θ^{+}	output angle of positive-sequence PLL
θ^{-}	output angle of negative-sequence PLL
$\omega_{\mathrm{pll}}^{+}$	output angular frequency of positive-sequence PLL
$\omega_{\mathrm{pll}}^{-}$	output angular frequency of negative-sequence PLL
U_{dc}	DC-link voltage of DFIG
δ^{+}	angle difference between $\boldsymbol{U}_{\mathrm{s}}^{+}$ and $\boldsymbol{U}_{\mathrm{gf}}^{+}$
δ^{-}	angle difference between $\boldsymbol{U}_{\mathrm{s}}^{-}$ and $\boldsymbol{U}_{\mathrm{gf}}^{-}$

C. Subscripts

$d\pm$, $q\pm$	$d\pm/q\pm$ axis component
r, s, g	rotor, stator, and grid-side converter
f	values during low voltage ride through

D. Superscripts

$\pm$	PS and NS component
*	reference value

I. Introduction

Recently, renewable energy generation technologies, particularly wind power, have grown rapidly worldwide due to their wide availability, extensive distribution, and environmental friendliness [1]. However, many renewable energy power farms (REPFs) are located in remote areas, where grid voltages are susceptible to asymmetrical drops caused by unbalanced three-phase loads or short-circuit faults. Given the limited anti-interference capability of power electronic devices, the complex voltage characteristics during faults can substantially affect the transient stability (TS) of REPF systems [2]. In particular, phase-locked loop (PLL)-based doubly-fed induction generator (DFIG) systems, whose stator is directly connected to the grid, are prone to rotor over-current, DC-link over-voltage, and even the loss of synchronous phenomenon [3], [4]. Therefore, it is important to further investigate the transient behavior of PLL-based DFIG systems under asymmetrical grid faults.

TS of PLL-based DFIG systems under grid faults has been investigated. References [5]–[7] examine the transient synchronization characteristics of REPF during various stages of grid faults and outline the physical mechanisms that allow REPF systems to maintain transient synchronism with the grid. However, the impact of the transient behavior for DC-link voltage (DCV) on the TS characteristics of REPF systems has not been addressed in the studies. Since the DC-link capacitance in DFIG systems serves as a key energy storage element between the rotor side converter (RSC) and grid side converter (GSC) [8], [9], DCV may increase or decrease due to energy change in the DC capacitance during asymmetrical faults. Moreover, given that the control bandwidth of DCV is close to that of PLL [10], the dynamic behavior of DCV may further influence the TS of the PLL. Consequently, the instability of DCV can also induce transient instability for REPF systems.

To investigate the transient behavior of DCV in REPF during grid faults, references [11]–[13] explore the dynamic characteristics of DCV under grid fault conditions. However, these studies mainly focus on DCV behavior under symmetrical grid faults, whereas under asymmetrical grid faults, positive and negative sequence (PNS) components appear simultaneously in the DFIG system [14]. In addition, since the PNS networks are interconnected, the PNS components are coupled under asymmetrical faults [15]. Therefore, the transient characteristics for DCV in DFIG systems under asymmetrical grid faults are considerably more complex than symmetrical faults. Although previous work [16] has investigated the dynamic behavior of PNS components of REPF in PLL on the control timescale during asymmetrical faults, it did not consider the transient behavior of DCV. As a result, the transient response of the system during asymmetrical faults requires further investigation.

Furthermore, several control strategies have been proposed to improve the TS of DCV in REPF during grid faults. References [17]–[19] introduce adaptive control methods to mitigate DCV fluctuations under both asymmetrical and symmetric grid voltage faults. However, these strategies do not incorporate a dual-sequence PLL, making it difficult to accurately identify the dominant factors affecting the TS of DCV and thereby limiting the suppression of their effects. In addition, the role of the integrator is not addressed in these methods, which further limits the transient performance of DCV [20], [21]. Particularly, under severe grid faults, the ability of DCV to maintain TS is weak. Therefore, it is essential to further study the effect of the integrator on the transient characteristics of DCV and develop an effective control strategy that enhances the TS of DCV in DFIG systems under asymmetrical grid faults.

To address the gaps mentioned above, this paper further investigates the transient instability forms and the TS mechanism of DCV for the PLL-based grid-connected DFIG system under asymmetrical faults. Based on this analysis, a coordinated control strategy is proposed to enhance the TS of PLL-based DFIG systems during asymmetrical grid faults. The main contributions are summarized as follows.

1) A novel transient modeling method of DCV for DFIG systems during asymmetrical faults is presented, which takes into account the transient characteristics of DCV, the dynamic behaviors of PNS components, and their coupling relationships.

2) The instability mechanism for DCV during asymmetrical grid faults is revealed. In addition, the dominant factors that influence the TS level of DCV are identified through the use of the phase trajectory diagram.

3) Considering the latest grid codes and the current capacity limits of converters, this paper proposes a novel TS control strategy to enhance both the response characteristics and TS level of DCV during asymmetrical grid faults. This is achieved through power coordination control between the RSC and GSC.

The organization of the rest of the paper is as follows. Section II establishes the nonlinear transient model in the DCV control timescale, while Section III presents the TS mechanism of DCV during asymmetrical grid faults. Section IV introduced a coordinated control strategy of DCV during symmetrical grid faults, and Section V verifies the analysis through simulation and experimental results. Finally, Section VI provides the conclusions of the study.

II. Modeling of Grid-connected DFIG System in DCV Control Time Scale

During low-voltage ride-through (LVRT), to provide fast PNS reactive currents support to the system according to grid codes [22]–[24], the RSC of the DFIG system adopts the single current loop control strategy. Figure 1 illustrates the typical control diagram of a grid-connected PLL-based DFIG system during asymmetrical grid faults [15].

As shown in Fig. 1, the PLL-based DFIG system contains several physical energy storage components, including the rotor, the DC capacitance, and the AC inductance. Since the transient response of DCV is considerably slower than that of the inner current, most studies [6], [12], [24] disregard the influence of the dynamic characteristics of the current loop on system TS. Therefore, this paper assumes that the output current vectors of the GSC and RSC can instantaneously follow their reference values. In addition, the dynamic characteristics of the stator and rotor flux, as well as the power loss of the DFIG system, are also neglected [14].

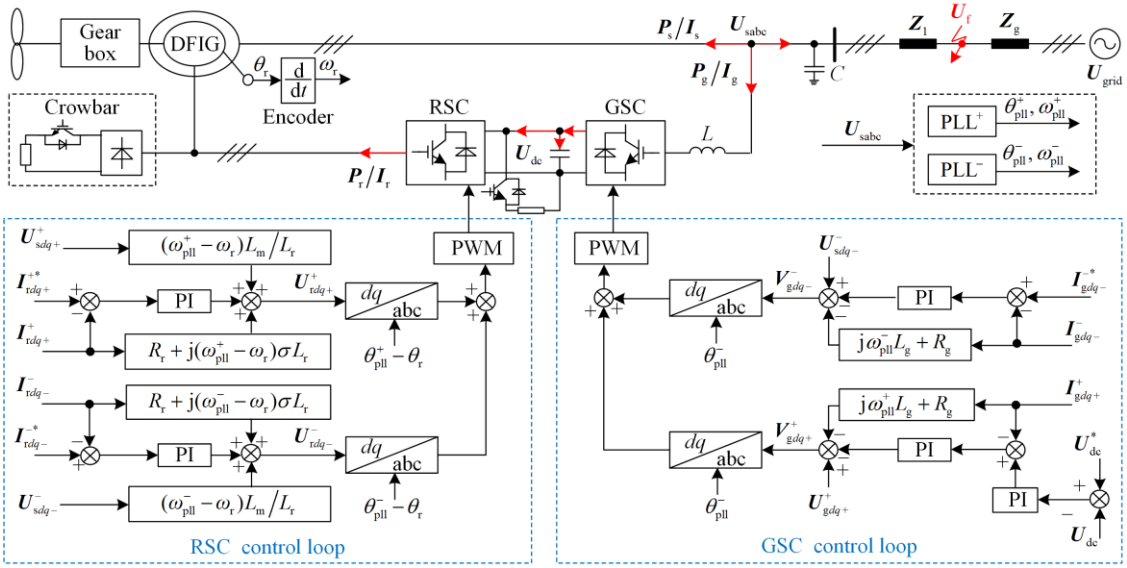

Fig. 1. Typical control structure of a PLL-based DFIG system during asymmetrical faults.

To further investigate the dynamic coupling behaviors of the PNS components [25] in the DFIG system within the DCV control timescale under asymmetrical faults, this paper establishes a dual-sequence synchronization large signal model in the PNS synchronous reference frames ($dq\pm$), as shown as Fig. 2.

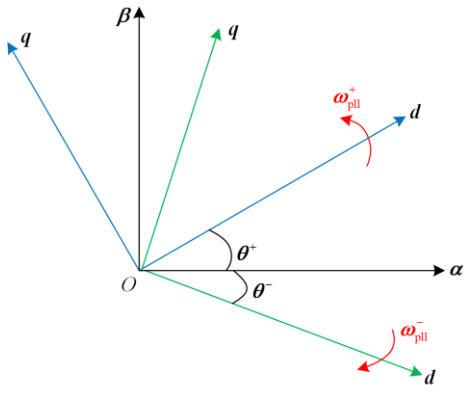

Fig. 2. PNS synchronous reference frames.

To ensure accurate tracking of the PNS voltage of the system, the PNS dual-sequence PLL control scheme proposed in [16] is adopted. Furthermore, the method introduced in [26] is applied to extract the PNS voltage components separately. According to [16], the voltage and flux equations of the DFIG system in $dq\pm$ are:

$$\begin{cases} \boldsymbol{U}^{+}_{sdq+} = -R_s \boldsymbol{I}^{+}_{sdq+} + \dfrac{\mathrm{d}\boldsymbol{\Psi}^{+}_{sdq+}}{\mathrm{d}t} + \mathrm{j}\omega^{+}_{\mathrm{pll}}\boldsymbol{\Psi}^{+}_{sdq+} \\ \boldsymbol{U}^{+}_{rdq+} = R_r \boldsymbol{I}^{+}_{rdq+} + \dfrac{\mathrm{d}\boldsymbol{\Psi}^{+}_{rdq+}}{\mathrm{d}t} + \mathrm{j}\left(\omega^{+}_{\mathrm{pll}} - \omega_r\right)\boldsymbol{\Psi}^{+}_{rdq+} \\ \boldsymbol{U}^{-}_{sdq-} = -R_s \boldsymbol{I}^{-}_{sdq-} + \dfrac{\mathrm{d}\boldsymbol{\Psi}^{-}_{sdq-}}{\mathrm{d}t} + \mathrm{j}\omega^{-}_{\mathrm{pll}}\boldsymbol{\Psi}^{-}_{sdq-} \\ \boldsymbol{U}^{-}_{rdq-} = R_r \boldsymbol{I}^{-}_{rdq-} + \dfrac{\mathrm{d}\boldsymbol{\Psi}^{-}_{rdq-}}{\mathrm{d}t} + \mathrm{j}\left(\omega^{-}_{\mathrm{pll}} - \omega_r\right)\boldsymbol{\Psi}^{-}_{rdq-} \end{cases} \tag{1}$$

$$\begin{cases} \boldsymbol{\Psi}^{+}_{sdq+} = -L_s \boldsymbol{I}^{+}_{sdq+} + L_m \boldsymbol{I}^{+}_{rdq+} \\ \boldsymbol{\Psi}^{+}_{rdq+} = -L_m \boldsymbol{I}^{+}_{sdq+} + L_r \boldsymbol{I}^{+}_{rdq+} \\ \boldsymbol{\Psi}^{-}_{sdq-} = -L_s \boldsymbol{I}^{-}_{sdq-} + L_m \boldsymbol{I}^{-}_{rdq-} \\ \boldsymbol{\Psi}^{-}_{rdq-} = -L_m \boldsymbol{I}^{-}_{sdq-} + L_r \boldsymbol{I}^{-}_{rdq-} \end{cases} \tag{2}$$

A. Dual-sequence Synchronous Model of the DFIG System

During the pre-fault stage, the DFIG system operates under maximum power point tracking (MPPT) and unity power factor mode. When an asymmetrical short-circuit fault occurs, the voltage of the stator $\boldsymbol{U}_s$ is given as:

$$\boldsymbol{U}_{\mathrm{s}}=\begin{cases}\boldsymbol{U}_{\mathrm{sN}}\mathrm{e}^{\mathrm{j}\omega_{\mathrm{g}}t}, & t<t_0\\ \boldsymbol{U}_{\mathrm{s}}^{+}\mathrm{e}^{\mathrm{j}\omega_{\mathrm{pll}}^{+}t}+\boldsymbol{U}_{\mathrm{s}}^{-}\mathrm{e}^{\mathrm{j}\omega_{\mathrm{pll}}^{-}t}, & t\geqslant t_0\end{cases} \tag{3}$$

where $\boldsymbol{U}_{\mathrm{sN}}$ represents the rated stator voltage; while $\boldsymbol{U}_{\mathrm{s}}^{+}$ and $\boldsymbol{U}_{\mathrm{s}}^{-}$ are the PNS components of the stator voltage during faults, respectively.

By neglecting the stator resistance R_{s} and combining (1)–(3), the relationships between stator and rotor current can be obtained as:

$$\begin{cases}\boldsymbol{I}_{\mathrm{sd}+}^{+}=\dfrac{L_{\mathrm{m}}}{L_{\mathrm{s}}}\boldsymbol{I}_{\mathrm{rd}+}^{+}\\ \boldsymbol{I}_{\mathrm{sq}+}^{+}=\dfrac{1}{L_{\mathrm{s}}}\left(L_{\mathrm{m}}\boldsymbol{I}_{\mathrm{rq}+}^{+}+\dfrac{|\boldsymbol{U}_{\mathrm{s}}^{+}|}{\omega_{\mathrm{pll}}^{+}}\right)\\ \boldsymbol{I}_{\mathrm{sd}-}^{-}=\dfrac{L_{\mathrm{m}}}{L_{\mathrm{s}}}\boldsymbol{I}_{\mathrm{rd}-}^{-}\\ \boldsymbol{I}_{\mathrm{sq}-}^{-}=\dfrac{1}{L_{\mathrm{s}}}\left(L_{\mathrm{m}}\boldsymbol{I}_{\mathrm{rq}-}^{-}+\dfrac{|\boldsymbol{U}_{\mathrm{s}}^{-}|}{\omega_{\mathrm{pll}}^{-}}\right)\end{cases} \tag{4}$$

Similarly, the mathematical model of the GSC under asymmetrical faults can be delivered as:

$$\begin{cases}\boldsymbol{U}_{\mathrm{gdq}+}^{+}=\boldsymbol{V}_{\mathrm{gdq}+}^{+}+\left(\mathrm{j}\omega_{\mathrm{pll}}^{+}L_{\mathrm{g}}+R_{\mathrm{g}}\right)\boldsymbol{I}_{\mathrm{gdq}+}^{+}+L_{\mathrm{g}}\dfrac{\mathrm{d}\boldsymbol{I}_{\mathrm{gdq}+}^{+}}{\mathrm{d}t}\\ \boldsymbol{U}_{\mathrm{gdq}-}^{-}=\boldsymbol{V}_{\mathrm{gdq}-}^{-}+\left(\mathrm{j}\omega_{\mathrm{pll}}^{-}L_{\mathrm{g}}+R_{\mathrm{g}}\right)\boldsymbol{I}_{\mathrm{gdq}-}^{-}+L_{\mathrm{g}}\dfrac{\mathrm{d}\boldsymbol{I}_{\mathrm{gdq}-}^{-}}{\mathrm{d}t}\end{cases} \tag{5}$$

B. Transient Model in the DCV Control Timescale

In Fig. 1, the governing equation of the DCV can be expressed as:

$$C\frac{\mathrm{d}U_{\mathrm{dc}}}{\mathrm{d}t}=\frac{P_{\mathrm{g}}}{U_{\mathrm{dc}}}-\frac{P_{\mathrm{r}}}{U_{\mathrm{dc}}} \tag{6}$$

where P_{s} is the active power absorbed by GSC; while P_{r} is the active power released by RSC; and C is the value of DC-link capacitor.

According to [11], the relationship between P_{g} and P_{r} is:

$$\begin{cases}P_{\mathrm{r}+}=s_1P_{\mathrm{s}+}\\ P_{\mathrm{r}-}=s_2P_{\mathrm{s}-}\\ s_1=\left(\omega_{\mathrm{pll}}^{+}-\omega_{\mathrm{g}}\right)/\omega_{\mathrm{pll}}^{+}\\ s_2=\left(\omega_{\mathrm{pll}}^{-}-\omega_{\mathrm{g}}\right)/\omega_{\mathrm{pll}}^{+}\end{cases} \tag{7}$$

The stator power of the DFIG system is:

$$\boldsymbol{S}_{\mathrm{s}}=\frac{3}{2}\left(\boldsymbol{U}_{\mathrm{sdq}+}^{+}\mathrm{e}^{\mathrm{j}\omega_{\mathrm{pll}}^{+}t}+\boldsymbol{U}_{\mathrm{sdq}-}^{-}\mathrm{e}^{\mathrm{j}\omega_{\mathrm{pll}}^{-}t}\right)\times\left(\boldsymbol{I}_{\mathrm{sdq}+}^{+}\mathrm{e}^{\mathrm{j}\omega_{\mathrm{pll}}^{+}t}+\boldsymbol{I}_{\mathrm{sdq}-}^{-}\mathrm{e}^{\mathrm{j}\omega_{\mathrm{pll}}^{-}t}\right) \tag{8}$$

Based on (8), P_{s} can be written as:

$$P_{\mathrm{s}}=\frac{3}{2}\begin{bmatrix}u_{\mathrm{sd}+}^{+}i_{\mathrm{sd}+}^{+}+u_{\mathrm{sd}-}^{-}i_{\mathrm{sd}-}^{-}+u_{\mathrm{sq}+}^{+}i_{\mathrm{sq}+}^{+}+u_{\mathrm{sq}-}^{-}i_{\mathrm{sq}-}^{-}+\\ \left(u_{\mathrm{sd}-}^{-}i_{\mathrm{sd}+}^{+}+u_{\mathrm{sq}-}^{-}i_{\mathrm{sq}+}^{+}+u_{\mathrm{sd}+}^{+}i_{\mathrm{sd}-}^{-}+u_{\mathrm{sq}+}^{+}i_{\mathrm{sq}-}^{-}\right)\cos(\theta^{+}+\theta^{-})+\\ \left(u_{\mathrm{sq}-}^{-}i_{\mathrm{sd}+}^{+}-u_{\mathrm{sd}-}^{-}i_{\mathrm{sq}+}^{+}-u_{\mathrm{sq}+}^{+}i_{\mathrm{sd}-}^{-}+u_{\mathrm{sd}+}^{+}i_{\mathrm{sq}-}^{-}\right)\sin(\theta^{+}+\theta^{-})\end{bmatrix} \tag{9}$$

Substituting (4) into (9) yields:

$$P_{\mathrm{r}}=\frac{3L_{\mathrm{m}}}{2L_{\mathrm{s}}}\times\begin{bmatrix}\begin{pmatrix}u_{\mathrm{sd}+}^{+}+u_{\mathrm{sd}-}^{-}\cos\left(\theta^{+}+\theta^{-}\right)+\\ u_{\mathrm{sq}-}^{-}\sin\left(\theta^{+}+\theta^{-}\right)\end{pmatrix}\times s_1i_{\mathrm{rd}+}^{+*}+\\ \begin{pmatrix}u_{\mathrm{sq}+}^{+}+u_{\mathrm{sq}-}^{-}\cos\left(\theta^{+}+\theta^{-}\right)-\\ u_{\mathrm{sd}-}^{-}\sin\left(\theta^{+}+\theta^{-}\right)\end{pmatrix}\times\left(i_{\mathrm{rq}+}^{+}+\dfrac{|U_{\mathrm{s}}^{+}|}{L_{\mathrm{m}}\omega_{\mathrm{pll}}^{+}}\right)s_1+\\ \begin{pmatrix}u_{\mathrm{sd}-}^{-}+u_{\mathrm{sd}+}^{+}\cos\left(\theta^{+}+\theta^{-}\right)-\\ u_{\mathrm{sq}+}^{+}\sin\left(\theta^{+}+\theta^{-}\right)\end{pmatrix}\times s_2i_{\mathrm{rd}-}^{-*}+\\ \begin{pmatrix}u_{\mathrm{sq}-}^{-}+u_{\mathrm{sq}+}^{+}\cos\left(\theta^{+}+\theta^{-}\right)+\\ u_{\mathrm{sd}+}^{+}\sin\left(\theta^{+}+\theta^{-}\right)\end{pmatrix}\times\left(i_{\mathrm{rq}-}^{-}+\dfrac{|U_{\mathrm{s}}^{-}|}{L_{\mathrm{m}}\omega_{\mathrm{pll}}^{-}}\right)s_2\end{bmatrix} \tag{10}$$

Similarly, P_{g} is derived as:

$$P_{\mathrm{g}}=\frac{3}{2}\times\begin{bmatrix}u_{\mathrm{sd}+}^{+}i_{\mathrm{gd}+}^{+}+u_{\mathrm{sd}-}^{-}i_{\mathrm{gd}-}^{-}+u_{\mathrm{gq}+}^{+}i_{\mathrm{sq}+}^{+}+u_{\mathrm{gq}-}^{-}i_{\mathrm{sq}-}^{-}+\\ \begin{pmatrix}u_{\mathrm{sd}-}^{-}i_{\mathrm{gd}+}^{+}+u_{\mathrm{sq}-}^{-}i_{\mathrm{gq}+}^{+}+\\ u_{\mathrm{sd}+}^{+}i_{\mathrm{gd}-}^{-}+u_{\mathrm{sq}+}^{+}i_{\mathrm{gq}-}^{-}\end{pmatrix}\times\cos\left(\theta^{+}+\theta^{-}\right)+\\ \begin{pmatrix}u_{\mathrm{sq}-}^{-}i_{\mathrm{gd}+}^{+}-u_{\mathrm{sd}-}^{-}i_{\mathrm{gq}+}^{+}-\\ u_{\mathrm{sq}+}^{+}i_{\mathrm{gd}-}^{-}+u_{\mathrm{sd}+}^{+}i_{\mathrm{gq}-}^{-}\end{pmatrix}\times\sin\left(\theta^{+}+\theta^{-}\right)\end{bmatrix} \tag{11}$$

where u_{s} is equal to u_{g}.

Combined with (7)–(11), equation (6) can be expressed as:

$$\begin{aligned}&\frac{2CL_{\mathrm{s}}U_{\mathrm{dc}}}{3L_{\mathrm{m}}}\frac{\mathrm{d}U_{\mathrm{dc}}}{\mathrm{d}t}=\\ &\begin{pmatrix}u_{\mathrm{sd}+}^{+}+u_{\mathrm{sd}-}^{-}\cos\left(\theta^{+}+\theta^{-}\right)-\\ u_{\mathrm{sq}-}^{-}\sin\left(\theta^{+}+\theta^{-}\right)\end{pmatrix}\times\left(\frac{L_{\mathrm{s}}}{L_{\mathrm{m}}}i_{\mathrm{gd}+}^{+*}-s_1i_{\mathrm{rd}+}^{+*}\right)+\\ &\begin{pmatrix}u_{\mathrm{sq}+}^{+}+u_{\mathrm{sq}-}^{-}\cos\left(\theta^{+}+\theta^{-}\right)-\\ u_{\mathrm{sd}-}^{-}\sin\left(\theta^{+}+\theta^{-}\right)\end{pmatrix}\times\left(\frac{L_{\mathrm{s}}}{L_{\mathrm{m}}}i_{\mathrm{gq}+}^{+*}-\left(i_{\mathrm{rq}+}^{+*}+\frac{|U_{\mathrm{s}}^{+}|}{L_{\mathrm{m}}\omega_{\mathrm{pll}}^{+}}\right)s_1\right)+\\ &\begin{pmatrix}u_{\mathrm{sd}-}^{-}+u_{\mathrm{sd}+}^{+}\cos\left(\theta^{+}+\theta^{-}\right)-\\ u_{\mathrm{sq}+}^{+}\sin\left(\theta^{+}+\theta^{-}\right)\end{pmatrix}\times\left(\frac{L_{\mathrm{s}}}{L_{\mathrm{m}}}i_{\mathrm{gd}-}^{-*}-s_2i_{\mathrm{rd}-}^{-*}\right)+\\ &\begin{pmatrix}u_{\mathrm{sq}-}^{-}+u_{\mathrm{sq}+}^{+}\cos\left(\theta^{+}+\theta^{-}\right)+\\ u_{\mathrm{sd}+}^{+}\sin\left(\theta^{+}+\theta^{-}\right)\end{pmatrix}\times\left(\frac{L_{\mathrm{s}}}{L_{\mathrm{m}}}i_{\mathrm{gq}-}^{-*}-\left(i_{\mathrm{rq}-}^{-*}+\frac{|U_{\mathrm{s}}^{-}|}{L_{\mathrm{m}}\omega_{\mathrm{pll}}^{-}}\right)s_2\right)\end{aligned} \tag{12}$$

Considering that the presence of the integrator limits the transient performance of the PLL-based DFIG system during grid faults [20], [21], i_{gd}^{*+} can be obtained through proportional control of the DCV deviation [11], described as:

$$i_{\mathrm{gd}+}^{+*}=k_{\mathrm{dc}}\left(U_{\mathrm{dc}}^{*}-U_{\mathrm{dc}}\right) \tag{13}$$

Substituting (13) into (12) yields:

$$
\begin{cases}
J_{\mathrm{c}}\dfrac{\mathrm{d}U_{\mathrm{dc}}}{\mathrm{d}t}=-P_{\mathrm{D}}+P_{\mathrm{so}}-P_{\mathrm{do}} \\
J_{\mathrm{c}}=\dfrac{2}{3}\dfrac{L_{\mathrm{s}}}{L_{\mathrm{m}}}CU_{\mathrm{dc}} \\
P_{\mathrm{D}}=D_{\mathrm{c}}\times\left(U_{\mathrm{dc}}-U_{\mathrm{dc}}^{*}\right) \\
D_{\mathrm{c}}=\dfrac{L_{\mathrm{s}}}{L_{\mathrm{m}}}k_{\mathrm{dc}}\left(u_{sd+}^{+}+u_{sd-}^{-}\cos\left(\theta^{+}+\theta^{-}\right)\right) \\
P_{\mathrm{so}}=\left(u_{sd-}^{-}+u_{sd+}^{+}\cos\left(\theta^{+}+\theta^{-}\right)\right)\times\left(\dfrac{L_{\mathrm{s}}}{L_{\mathrm{m}}}i_{gd-}^{-*}-s_2 i_{rd-}^{-*}\right)+ \\
\quad\left(u_{sd+}^{+}\sin\left(\theta^{+}+\theta^{-}\right)\right)\times\left(\dfrac{L_{\mathrm{s}}}{L_{\mathrm{m}}}i_{gq-}^{-*}-\left(i_{rq-}^{-*}+\dfrac{|U_{\mathrm{s}}^{-}|}{L_{\mathrm{m}}\omega_{\mathrm{pll}}^{-}}\right)s_2\right)- \\
\quad\left(u_{sd+}^{+}+u_{sd-}^{-}\cos\left(\theta^{+}+\theta^{-}\right)\right)\times s_1 i_{rd+}^{+*}- \\
\quad\left(u_{sd-}^{-}\sin\left(\theta^{+}+\theta^{-}\right)\right)\times\left(\dfrac{L_{\mathrm{s}}}{L_{\mathrm{m}}}i_{gq+}^{+*}-\left(i_{rq+}^{+*}+\dfrac{|U_{\mathrm{s}}^{+}|}{L_{\mathrm{m}}\omega_{\mathrm{pll}}^{+}}\right)s_1\right) \\
P_{\mathrm{do}}=\left(u_{sq-}^{-}+u_{sq+}^{+}\cos\left(\theta^{+}+\theta^{-}\right)\right)\times\left(\dfrac{L_{\mathrm{s}}}{L_{\mathrm{m}}}i_{gq-}^{-*}-\left(i_{rq-}^{-*}+\dfrac{|U_{\mathrm{s}}^{-}|}{L_{\mathrm{m}}\omega_{\mathrm{pll}}^{-}}\right)s_2\right)+ \\
\quad u_{sq-}^{-}\sin\left(\theta^{+}+\theta^{-}\right)\times\left(\dfrac{L_{\mathrm{s}}}{L_{\mathrm{m}}}i_{gd+}^{+*}-s_1 i_{rd+}^{+*}\right)+ \\
\quad\left(u_{sq+}^{+}+u_{sq-}^{-}\cos\left(\theta^{+}+\theta^{-}\right)\right)\times\left(\dfrac{L_{\mathrm{s}}}{L_{\mathrm{m}}}i_{gq+}^{+*}-\left(i_{rq+}^{+*}+\dfrac{|U_{\mathrm{s}}^{+}|}{L_{\mathrm{m}}\omega_{\mathrm{pll}}^{+}}\right)s_1\right)- \\
\quad u_{sq+}^{+}\sin\left(\theta^{+}+\theta^{-}\right)\times\left(\dfrac{L_{\mathrm{s}}}{L_{\mathrm{m}}}i_{gd-}^{-*}-s_2 i_{rd-}^{-*}\right)
\end{cases}
\tag{14}
$$

where P_{D} is the equivalent damping power; P_{so} is the equivalent static stable power; and P_{do} is the equivalent dynamic stable power; J_{c} denotes the equivalent inertia coefficient; and D_{c} denotes the equivalent damping coefficient of the DCV.

In (14), P_{do} represents the influence of the PLL control characteristics on DCV transient response, while P_{D} and P_{so} denote the influence of the power coordination control characteristics between the RSC and GSC on DCV transient behavior. In addition, equation (14) shows that the DCV transient characteristics are also influenced by the control parameter k_{dc}, the DC-link capacitance C, s_1, and s_2. Accordingly, the phase trajectories of the DCV under different control parameters are illustrated in Figs. 3 and 4, where A^{+} and A^{-} are the initial points of the system.

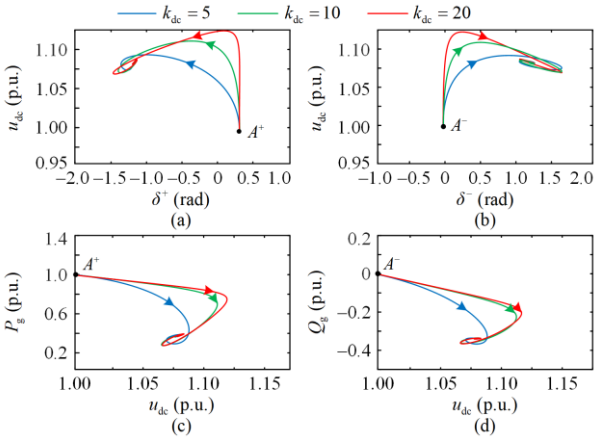

Fig. 3. Influence of the proportional coefficient in the DCV control loop. (a) Phase trajectories of DCV and PS equivalent power angle. (b) Phase trajectories of DCV and negative sequence (NS) equivalent power angle. (c) Phase trajectories of DCV and active power. (d) Phase trajectories of DCV and reactive power.

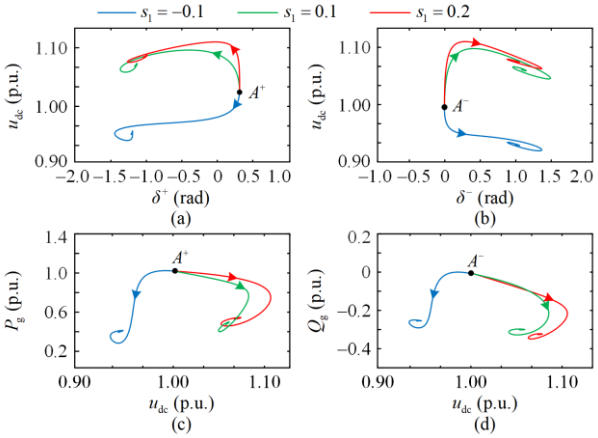

Fig. 4. Influence of s_1. (a) Phase trajectories of DCV and PS equivalent power angle. (b) Phase trajectories of DCV and NS equivalent power angle. (c) Phase trajectories of DCV and active power. (d) Phase trajectories of DCV and reactive power.

In Figs. 3 and 4, the LVRT current references of the RSC and GSC are 0.15 p.u., −0.35 p.u., −0.05 p.u., −0.45 p.u., 0, 0, and 0. The results show that although the DCV transient characteristics are significantly influenced by k_{dc} and s_1, the DCV cannot be restored to U_{dc0} solely by adjusting the system control parameters. Furthermore, the dynamic behavior of the DCV has a considerable impact on the power output of the DFIG system, which cannot be overlooked.

Figure 5 illustrates the phase trajectories diagram of DCV under different DC-link capacitance values. Although increasing the DC-link capacitance allows the DCV to reach a transiently stable state more quickly, the DCV cannot be restored to U_{dc0} simply by adjusting the capacitance value. Similarly, as demonstrated in Figs. 6–9, by increasing the proportional coefficient or decreasing the integration coefficient of the PNS PLL, the PNS equivalent power angles, and the DCV can return to

transiently stable states more quickly, yet the DCV still cannot be restored to U_{dc0}. Therefore, it is essential to further analyze the transient behavior of the DCV during asymmetrical faults, identify the dominant factors that influence the TS of the DCV, and study the control strategy aimed at enhancing the TS of the DCV.

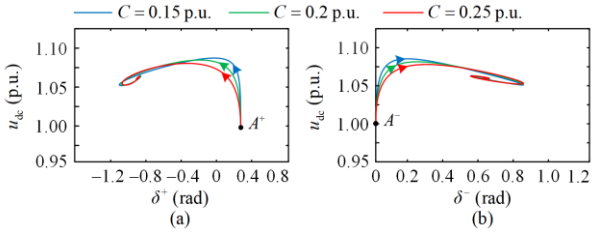

Fig. 5. Influence of DC-link capacitance. (a) Phase trajectories of DCV and PS equivalent power angle. (b) Phase trajectories of DCV and NS equivalent power angle.

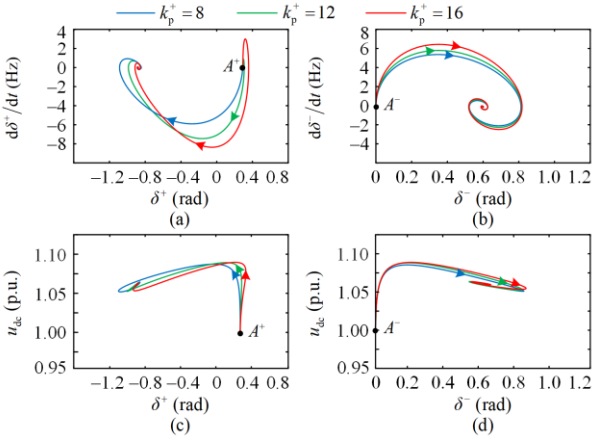

Fig. 6. Influence of the proportional coefficient of PS PLL. (a) Phase trajectories diagram of δ^+ and $\mathrm{d}\delta^+/\mathrm{d}t$. (b) Phase trajectories of δ^- and $\mathrm{d}\delta^-/\mathrm{d}t$. (c) Phase trajectories of DCV and PS equivalent power angle. (d) Phase trajectories of DCV and NS equivalent power angle.

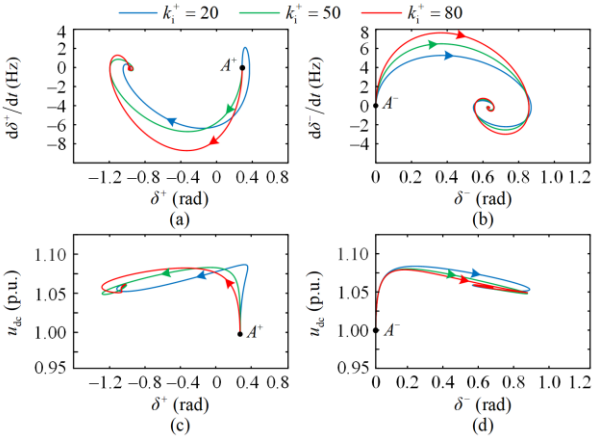

Fig. 7. Influence of the integration coefficient of PS PLL. (a) Phase trajectories diagram of δ^+ and $\mathrm{d}\delta^+/\mathrm{d}t$. (b) Phase trajectories of δ^- and $\mathrm{d}\delta^-/\mathrm{d}t$. (c) Phase trajectories of DCV and PS equivalent power angle. (d) Phase trajectories of DCV and NS equivalent power angle.

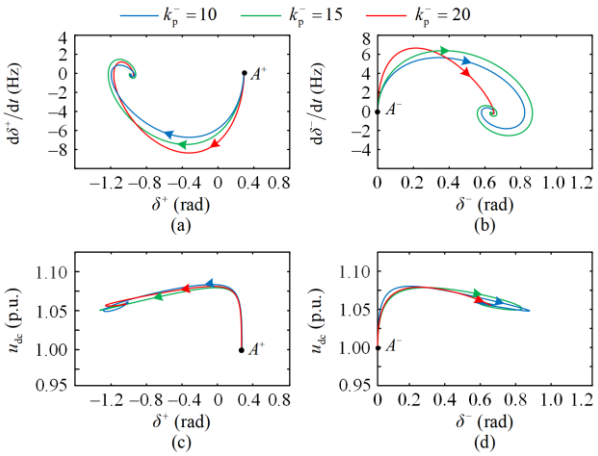

Fig. 8. Influence of the proportional coefficient of NS PLL. (a) Phase trajectories diagram of δ^+ and $\mathrm{d}\delta^+/\mathrm{d}t$. (b) Phase trajectories of δ^- and $\mathrm{d}\delta^-/\mathrm{d}t$. (c) Phase trajectories of DCV and PS equivalent power angle. (d) Phase trajectories of DCV and NS equivalent power angle.

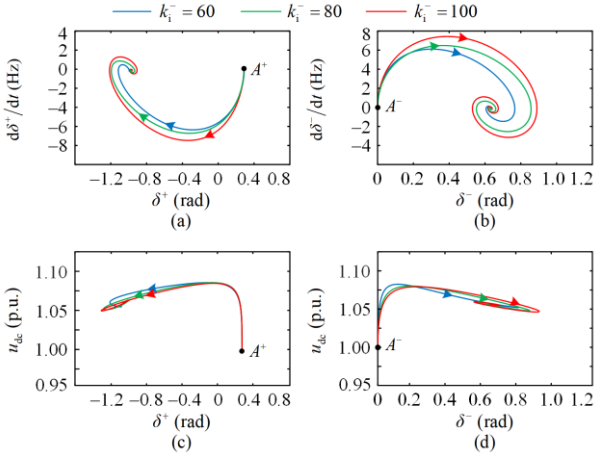

Fig. 9. Influence of the integration coefficient of the NS PLL. (a) Phase trajectories diagram of δ^+ and $\mathrm{d}\delta^+/\mathrm{d}t$. (b) Phase trajectories of δ^- and $\mathrm{d}\delta^-/\mathrm{d}t$. (c) Phase trajectories of DCV and PS equivalent power angle. (d) Phase trajectories of DCV and NS equivalent power angle.

III. Analysis of Transient Stability in the DCV Control Time Scale

Combining (1)–(14), the dynamic DCV control block diagram under asymmetrical faults can be obtained as shown in Fig. 10. The TS of DCV in the DFIG system is primarily influenced by the control characteristics of PLL, the coupling characteristics between the PNS components, and the coordinated power control between the RSC and GSC on the TS of DCV. Therefore, the mechanism of how these factors affecting the TS process and stability level of DCV will be further analyzed in this section.

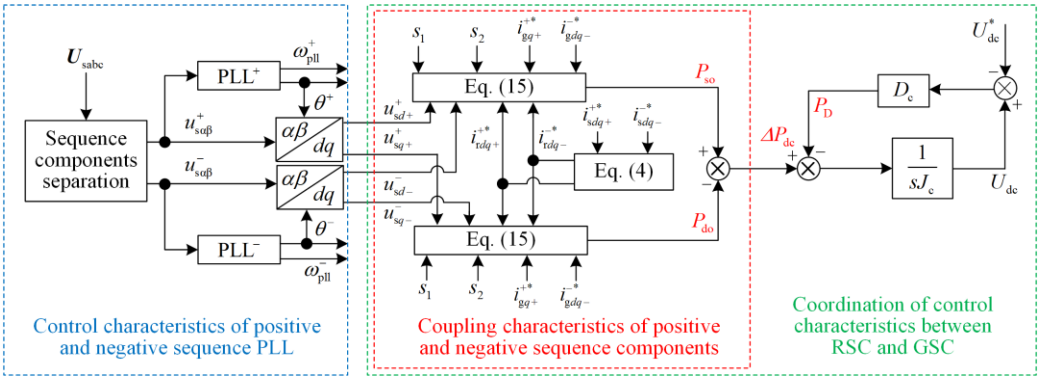

Fig. 10. Dynamic control block diagram of the DCV during asymmetrical faults.

A. Transient Stability Process of the DCV

According to Fig. 10, when an asymmetrical grid short-circuit fault occurs, the DFIG system switches to the LVRT control mode and adopts the single current loop control strategy. This results in a significant change in the output angular frequency of the PLL, which further leads to fluctuation in u^{+}_{sdq+} and u^{-}_{sdq-}. In this situation, based on (14), P_{do} is no longer equal to 0, and consequently, the power balance of the DC-link capacitance is disrupted, causing U_{dc} to deviate from U^{*}_{dc}. At the same time, the PLL suppresses the fluctuation of u^{+}_{sq+} and u^{-}_{sq-} to eliminate the interference P_{D}. In addition, under the influence of ΔU_{dc}, a signal will be generated by the DCV control loop to compensate for the unbalanced power caused by P_{so}, and prevent U_{dc} from diverging from U^{*}_{dc}. Ultimately, the DCV can be restored to a new stable state provided that the equilibrium point of the DFIG system exists.

From the above analysis, D_c acts in a manner similar to damping by preventing variation in DCV, while J_c influences the rate of change of DCV and can be regarded as the inertia coefficient. Therefore, the transient process of DCV in the DFIG system is comparable to that of a SG. Furthermore, as shown in Fig. 10, the PNS PLL mainly influences the power balance of the DC capacitor by regulating the terminal voltages u^{+}_{sdq+} and u^{-}_{sdq-}. The RSC and GSC primarily affect the power balance of the DC-link capacitor by controlling the output PNS currents.

B. Transient Stability Mechanism of the DCV

Based on the above analysis, if u^{+}_{sq+} and u^{-}_{sq-} cannot be fully regulated to 0 by the PLL, the disturbance of P_{do} will not be removed, thereby making the DCV unstable. Therefore, the main factors that cause instability of the DCV in the system can be classified as follows.

1) The Disturbance of P_{do} Cannot Be Eliminated

From Fig. 10 and (14), if u^{+}_{sq+} and u^{-}_{sq-} cannot be completely regulated to 0 by the PLL, the DCV will be unstable. Furthermore, since the PLL control characteristics are closely related to the dynamic behavior of the PNS equivalent power angles δ^{+} and δ^{-}, in the system, the DCV transient characteristics are also affected by the dynamic behavior of the PNS equivalent power angles. Therefore, it is necessary to analyze the relationship between the dynamic behaviors of the equivalent power angles and the transient process of DCV during asymmetrical grid faults. Equation (14) can be further written as:

$$
\begin{cases}
\dfrac{2CU_{dc}L_s}{3L_m}\times\dfrac{\mathrm{d}U_{dc}}{\mathrm{d}t}=-D_c\times\left(U_{dc}-U^{*}_{dc}\right)+P_{so+}-P_{do+}+P_{so-}-P_{do-}\\
P_{so+}=-u^{+}_{sd+}s_1i^{+*}_{rd+}+u^{+}_{sd+}\cos\left(\theta^{+}+\theta^{-}\right)\times\left(\dfrac{L_s}{L_m}i^{-*}_{gd-}-s_2i^{-*}_{rd-}\right)+\\
\qquad u^{+}_{sd+}\sin\left(\theta^{+}+\theta^{-}\right)\times\left(\dfrac{L_s}{L_m}i^{-*}_{gq-}-\left(i^{-*}_{rq-}+\dfrac{|U^{-}_{s}|}{L_m\omega^{-}_{pll}}\right)s_2\right)\\
P_{so-}=u^{-}_{sd-}\left(\dfrac{L_s}{L_m}i^{-*}_{gd-}-s_2i^{-*}_{rd-}\right)-u^{-}_{sd-}\cos\left(\theta^{+}+\theta^{-}\right)s_1i^{+*}_{rd+}-\\
\qquad u^{-}_{sd-}\sin\left(\theta^{+}+\theta^{-}\right)\times\left(\dfrac{L_s}{L_m}i^{+*}_{gq+}-i^{+*}_{rq+}-\dfrac{|U^{+}_{s}|}{L_m\omega^{+}_{pll}}\right)s_1\\
P_{do+}=u^{+}_{sq+}\left(\dfrac{L_s}{L_m}i^{+*}_{gq+}-\left(i^{+*}_{rq+}+\dfrac{|U^{+}_{s}|}{L_m\omega^{+}_{pll}}\right)s_1\right)-\\
\qquad u^{+}_{sq+}\sin\left(\theta^{+}+\theta^{-}\right)\times\left(\dfrac{L_s}{L_m}i^{-*}_{gd-}-s_2i^{-*}_{rd-}\right)+\\
\qquad u^{+}_{sq+}\cos\left(\theta^{+}+\theta^{-}\right)\times\left(\dfrac{L_s}{L_m}i^{-*}_{gq-}-\left(i^{-*}_{rq-}+\dfrac{|U^{-}_{s}|}{L_m\omega^{-}_{pll}}\right)s_2\right)\\
P_{do-}=u^{-}_{sq-}\left(\dfrac{L_s}{L_m}i^{-*}_{gq-}-\left(i^{-*}_{rq-}+\dfrac{|U^{-}_{s}|}{L_m\omega^{-}_{pll}}\right)s_2\right)+\\
\qquad u^{-}_{sq-}\sin\left(\theta^{+}+\theta^{-}\right)\times\left(\dfrac{L_s}{L_m}i^{+*}_{gd+}-s_1i^{+*}_{rd+}\right)+\\
\qquad u^{-}_{sq-}\cos\left(\theta^{+}+\theta^{-}\right)\times\left(\dfrac{L_s}{L_m}i^{+*}_{gq+}-\left(i^{+*}_{rq+}+\dfrac{|U^{+}_{s}|}{L_m\omega^{+}_{pll}}\right)s_1\right)
\end{cases}
\tag{15}
$$

Multiplying (15) by dt yields:

$$\begin{cases} \dfrac{2CU_{\mathrm{dc}}L_{\mathrm{s}}}{3L_{\mathrm{m}}}\mathrm{d}U_{\mathrm{dc}} = -D_{\mathrm{c}}\times\left(U_{\mathrm{dc}}-U_{\mathrm{dc}}^{*}\right)\mathrm{d}t + \\ \qquad\qquad \left(P_{\mathrm{so+}}-P_{\mathrm{do+}}+P_{\mathrm{so-}}-P_{\mathrm{do-}}\right)\mathrm{d}t \end{cases} \tag{16}$$

Since δ^{-} and δ^{-} can be expressed as [23]:

$$\begin{cases} \dfrac{\mathrm{d}\delta^{+}}{\mathrm{d}t} = \omega_{\mathrm{b}}\left(\omega_{\mathrm{pll}}^{+}-\omega_{\mathrm{g}}\right) \\ \dfrac{\mathrm{d}\delta^{-}}{\mathrm{d}t} = \omega_{\mathrm{b}}\left(\omega_{\mathrm{pll}}^{-}+\omega_{\mathrm{g}}\right) \end{cases} \tag{17}$$

Substitution of (17) into (16), followed by integration, yields:

$$\begin{aligned} &\left(\omega_{\mathrm{pll}}^{-}+\omega_{\mathrm{g}}\right)\left(\omega_{\mathrm{pll}}^{+}-\omega_{\mathrm{g}}\right)\underbrace{\frac{\omega_{\mathrm{b}}CL_{\mathrm{s}}}{3L_{\mathrm{m}}}\left(U_{\mathrm{dc}}^{2}-U_{\mathrm{dc0}}^{2}\right)}_{\Delta E_{\mathrm{K}}}+\left(\omega_{\mathrm{pll}}^{-}+\omega_{\mathrm{g}}\right)\times \\ &\underbrace{\int_{\delta_0^{+}}^{\delta^{+}} D_{\mathrm{c}}\left(U_{\mathrm{dc}}-U_{\mathrm{dc}}^{*}\right)\mathrm{d}\delta^{+}}_{\Delta E_{\mathrm{D}}}=\left(\omega_{\mathrm{pll}}^{-}+\omega_{\mathrm{g}}\right)\underbrace{\int_{\delta_0^{+}}^{\delta^{+}}\left(P_{\mathrm{so+}}-P_{\mathrm{do+}}\right)\mathrm{d}\delta^{+}}_{\Delta E_{\mathrm{P+}}}+ \\ &\left(\omega_{\mathrm{pll}}^{+}-\omega_{\mathrm{g}}\right)\underbrace{\int_{\delta_0^{-}}^{\delta^{-}}\left(P_{\mathrm{so-}}-P_{\mathrm{do-}}\right)\mathrm{d}\delta^{-}}_{\Delta E_{\mathrm{P-}}} \end{aligned} \tag{18}$$

where ΔE_{K} represents the equivalent kinetic energy of the DC-link capacitor during the transient process of DCV; U_{dc0} is the initial voltage of U_{dc}; $\Delta E_{\mathrm{P+}}$ and $\Delta E_{\mathrm{P-}}$ denote the equivalent potential energy generated by the PS and NS operating points during asymmetrical faults, respectively; and ΔE_{D} is the equivalent damping energy consumed by the DC-link capacitor.

According to the dynamic behaviors of δ^{+} and δ^{-} [11], two transient instability types of DCV can occur. When δ^{+} or δ^{-} increases monotonically during the faults, $P_{\mathrm{do+}}$ and $P_{\mathrm{do-}}$ will always exist. In this case, if $\Delta E<0$ ($\Delta E=\Delta E_{\mathrm{P+}}+\Delta E_{\mathrm{P-}}-\Delta E_{\mathrm{D}}$), the DC-link capacitor releases kinetic energy to compensate for ΔE, which results in a continuous decrease of DCV. If $\Delta E<0$, the DC-link capacitor reduces the excessive ΔE by increasing kinetic energy, leading to a continuous rise of DC voltage. However, when δ^{+} or δ^{-} decreases monotonically, if $\Delta E<0$, the DC capacitor absorbs the excessive ΔE, which results in a continuous increase of DCV. Conversely, when $\Delta E>0$, the DC-link capacitor releases kinetic energy to compensate for ΔE, which leads to a continuous decrease of DCV.

Based on the above analysis, the DCV can maintain TS only when P_{do} is eliminated. Therefore, the necessary condition for the DCV to maintain TS during asymmetrical grid faults is that both u_{sq+}^{+} and u_{sq-}^{-} are effectively regulated to 0, which requires the PS PLL and NS PLL to accurately track the PNS grid voltage of the DFIG system [23].

2) The Unbalanced Power Between P_{so} and P_{D} Cannot Be Eliminated

As illustrated in Fig. 10, although the existence of an equilibrium point in the DFIG system is the prerequisite for the DCV to remain TS during the asymmetrical grid faults, the TS level of the DCV is also affected by the power coordinated control characteristics between the RSC and GSC. Therefore, it is necessary to further investigate the influencing mechanism of the power coordinated control characteristics between the RSC and GSC on the TS level of the DCV.

Integrating both sides of (16) yields:

$$\begin{aligned} &\underbrace{\frac{L_{\mathrm{s}}C}{3L_{\mathrm{m}}}\left(U_{\mathrm{dc}}^{2}-U_{\mathrm{dc0}}^{2}\right)}_{\Delta W_{\mathrm{C}}}+\underbrace{\int_{t_0}^{t_1} D_{\mathrm{c}}\left(U_{\mathrm{dc}}-U_{\mathrm{dc}}^{*}\right)\mathrm{d}t}_{\Delta W_{\mathrm{D}}}= \\ &\underbrace{\int_{t_0}^{t_1}\left(P_{\mathrm{g\_so}}-P_{\mathrm{r\_so}}\right)\mathrm{d}t}_{\Delta W_{\mathrm{s}}}-\underbrace{\int_{t_0}^{t_1} P_{\mathrm{do}}\mathrm{d}t}_{\Delta W_{\mathrm{d}}} \end{aligned} \tag{19}$$

where t_0 is the initial moment of the fault; and t_1 is the moment when the fault recovers; ΔW_{C} denotes the energy accumulated or released by the DC capacitor during asymmetrical grid faults; ΔW_{D}, ΔW_{s}, and ΔW_{d} represent the energy produced by P_{D}, P_{so}, and P_{do}, respectively.

From (14) and (19), under the condition that u_{sq+}^{+} and u_{sq-}^{-} can be controlled to 0, P_{do} will remain 0 during asymmetrical grid faults, and no energy conversion caused by P_{do} will occur. Moreover, according to [11], if u_{sq+}^{+} and u_{sq-}^{-} can be controlled to 0, this implies that the equilibrium point of the system exists, and the negative D_{c} will not lead to DCV instability. Therefore, the DCV TS level during asymmetrical faults primarily depends on ΔW_{s}. By analyzing the interaction between $P_{\mathrm{g\_so}}$ and $P_{\mathrm{r\_so}}$, the following two DCV TS levels can be identified.

Case 1: When $P_{\mathrm{g\_so}}$ is greater than $P_{\mathrm{r\_so}}$, the energy absorbed by the GSC exceeds the energy released by the RSC during the faults, resulting in $\Delta W_{\mathrm{s}}>0$. In this case, the DC capacitor will be charged to balance the unbalanced energy ΔW_{s} which causes U_{dc} to be greater

than U_{dc0} during asymmetrical grid faults. Throughout this process, ΔW_D always remains greater than 0.

Case 2: During asymmetrical grid faults, if P_{g_so} is less than P_{r_so}, ΔW_s will be less than 0. In this case, the DC-link capacitor will discharge energy to offset the imbalance between the RSC and GSC, which leads to U_{dc} being less than U_{dc0}. Similarly, in this process, ΔW_D always remains greater than 0.

Based on the above analysis, the transient instability of the DCV in the DFIG system is primarily determined by the control characteristics of PLL during asymmetrical grid faults, while the DCV TS level is mainly influenced by the power coordinated control characteristics between the RSC and GSC.

IV. Transient Stability Coordinated Control Strategy of the DCV

According to the analysis in Section III, the necessary condition for the DCV to remain in TS during asymmetrical grid faults is that u_{sq+}^{+} and u_{sq-}^{-} can be controlled to 0. However, if this condition is satisfied, the unbalanced power coordinated control between the RSC and GSC can still affect the TS of the DCV. Therefore, to improve the DCV TS level and the TS of the DFIG, this section investigates the influence of different RSC active and reactive currents on the transient characteristics of the PNS equivalent power angles and DCV. Figures 11–14 illustrate the phase trajectories diagram of the DCV under different rotor PNS active and reactive current references.

As observed in Figs. 11–14, although the DCV TS level is not influenced by the PNS reactive current output by th RSC, the transient component of the DCV and the PS equivalent power angle increase progressively with the rise of the output PNS reactive current. This weakens the TS margin of the PS power angle and deteriorates the transient characteristics of DCV.

Furthermore, while a moderate increase in the PNS active current output by the RSC causes the DCV to exhibit different TS levels, the TS margin of the PNS equivalent power angle gradually improves, which enhances the overall TS margin of the system. However, an excessive PNS active current will reduce the TS margin of the system and may even result in system instability. Therefore, it is essential to properly coordinate the PNS active and reactive current of output by the RSC and GSC during asymmetrical grid faults. Otherwise, transient instability of the DCV and the system can occur.

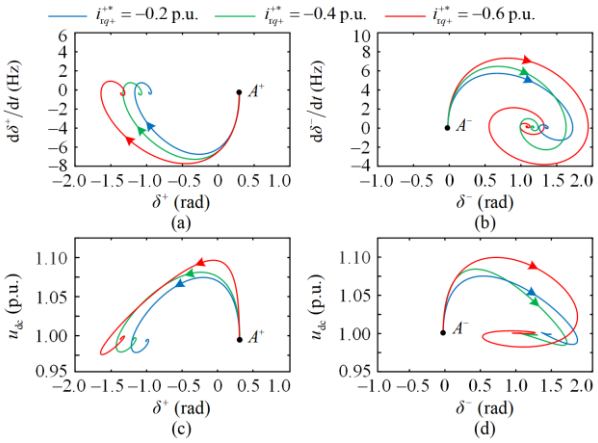

Fig. 11. Influence of rotor PS reactive current references. (a) Phase trajectories diagram of δ^+ and $d\delta^+/dt$. (b) Phase trajectories of δ^- and $d\delta^-/dt$. (c) Phase trajectories of DCV and PS equivalent power angle. (d) Phase trajectories of DCV and NS equivalent power angle.

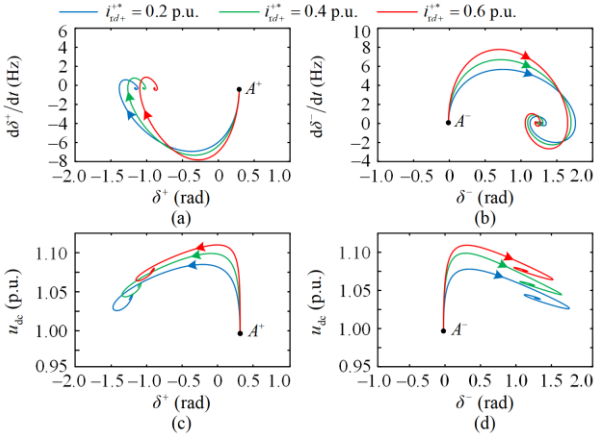

Fig. 12. Influence of rotor PS active current references. (a) Phase trajectories diagram of δ^+ and $d\delta^+/dt$. (b) Phase trajectories of δ^- and $d\delta^-/dt$. (c) Phase trajectories of DCV and PS equivalent power angle. (d) Phase trajectories of DCV and NS equivalent power angle.

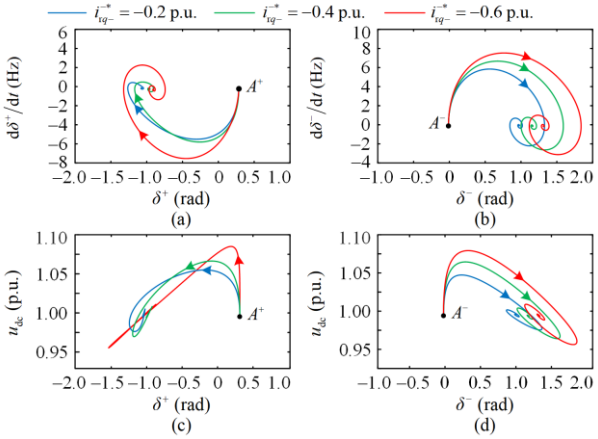

Fig. 13. Influence of rotor NS reactive current references. (a) Phase trajectories diagram of δ^+ and $d\delta^+/dt$. (b) Phase trajectories of δ^- and $d\delta^-/dt$. (c) Phase trajectories of DCV and PS equivalent power angle. (d) Phase trajectories of DCV and NS equivalent power angle.

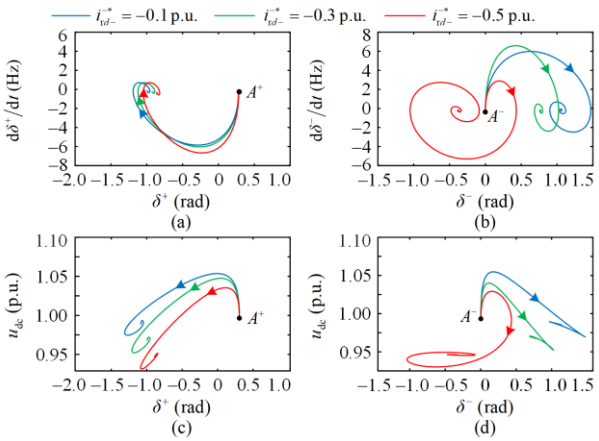

Fig. 14. Influence of rotor NS active current references. (a) Phase trajectories diagram of δ^+ and $d\delta^+/dt$. (b) Phase trajectories of δ^- and $d\delta^-/dt$. (c) phase trajectories of DCV and PS equivalent power angle. (d) Phase trajectories of DCV and NS equivalent power angle.

Considering the requirement of the latest grid codes [18], the output PNS reactive power currents i_{q+}^{+} and i_{q-}^{-} during asymmetrical grid faults must satisfy the followings:

$$\begin{cases} i_{q+}^{+} = -K^{+}\left(0.9-U_{\mathrm{s}}^{+}\right)I_{\mathrm{N}}, \quad 0.6 \leqslant U_{\mathrm{s}}^{+} \leqslant 0.9 \\ i_{q-}^{-} = -K^{-}U_{\mathrm{s}}^{-}I_{\mathrm{N}} \end{cases} \tag{20}$$

where K^+ is the PS reactive current proportional coefficient of the REPF; K^- is the NS reactive current proportional coefficient of the REPF; and I_{N} is the rated current of the REPF.

According to (14), to restore the DCV to a stable state, the equivalent damping power P_{D} must compensate for the fluctuations generated by the static stable power P_{so}. Since P_{D} is produced by ΔU_{dc}, while neither u_{sd+}^{+} nor u_{sd-}^{-} equals 0 during asymmetrical grid faults, the DCV fluctuation caused by P_{so} can only be eliminated by coordinating LVRT current references (i_{rdq+}^{+*}, i_{rdq-}^{-*}, i_{gdq+}^{+*}, and i_{gdq-}^{-*}) of the RSC and GSC. Therefore, the following equation can be obtained:

$$\begin{cases} \dfrac{L_{\mathrm{s}}}{L_{\mathrm{m}}}k_{\mathrm{dc}}\left(U_{\mathrm{dc}}^{*}-U_{\mathrm{dc}}\right)+\dfrac{L_{\mathrm{s}}}{L_{\mathrm{m}}}i_{gd-}^{-*}-s_1 i_{\mathrm{rd}+}^{+*}-s_2 i_{\mathrm{rd}-}^{-*}=0 \\ \dfrac{L_{\mathrm{s}}}{L_{\mathrm{m}}}i_{gq+}^{+*}-s_1\left(i_{\mathrm{rq}+}^{+*}+\dfrac{U_{\mathrm{s}}^{+}}{L_{\mathrm{m}}\omega_{\mathrm{pll}}^{+}}\right)=0 \\ \dfrac{L_{\mathrm{s}}}{L_{\mathrm{m}}}i_{gq-}^{-*}-s_2\left(i_{\mathrm{rq}-}^{-*}+\dfrac{U_{\mathrm{s}}^{-}}{L_{\mathrm{m}}\omega_{\mathrm{pll}}^{-}}\right)=0 \end{cases} \tag{21}$$

As a result, the coordinated control method of the PNS reactive currents for the RSC and GSC under asymmetrical grid faults is expressed as:

$$\begin{cases} i_{rq+}^{+*}=\dfrac{K^{+}\left(0.9-U_{\mathrm{s}}^{+}\right)I_{\mathrm{N}}L_{\mathrm{s}}}{L_{\mathrm{m}}\left(1+s_1\right)}-\dfrac{U_{\mathrm{s}}^{+}}{L_{\mathrm{m}}\omega_{\mathrm{pll}}^{+}}, \ 0.6 \leqslant U_{\mathrm{s}}^{+} \leqslant 0.9 \\ i_{rq-}^{-*}=\dfrac{K^{-}U_{\mathrm{s}}^{-}I_{\mathrm{N}}L_{\mathrm{s}}}{L_{\mathrm{m}}\left(1+s_2\right)}-\dfrac{U_{\mathrm{s}}^{-}}{L_{\mathrm{m}}\omega_{\mathrm{pll}}^{-}} \\ i_{gq+}^{+*}=\dfrac{s_1K^{+}\left(0.9-U_{\mathrm{s}}^{+}\right)I_{\mathrm{N}}}{1+s_1} \\ i_{gq-}^{-*}=\dfrac{s_2K^{-}U_{\mathrm{s}}^{-}I_{\mathrm{N}}}{1+s_2} \end{cases} \tag{22}$$

Considering that the grid codes [21]–[23] do not require the NS active current (i_{d-}^{-}) for the REPF, i_{d-}^{-} is set to 0 in this paper.

By substituting (22) into (19), the PNS active current under asymmetrical faults can be obtained on the condition that the equilibrium point of the system exists. In this situation, the optimal distribution strategy of the PNS active currents for the RSC and GSC during asymmetrical faults can be expressed as:

$$\begin{cases} i_{\mathrm{rd}+}^{+*}=-\dfrac{L_{\mathrm{s}}i_{d+}^{+}}{L_{\mathrm{m}}\left(1+s_1\right)} \\ i_{gd+}^{+*}=k_{\mathrm{dc}}\left(U_{\mathrm{dc}}^{*}-U_{\mathrm{dc}}\right)+s_1 i_{\mathrm{rd}+}^{+} \\ i_{\mathrm{rd}-}^{-*}=-\dfrac{L_{\mathrm{s}}i_{d-}^{-}}{L_{\mathrm{m}}\left(1+s_2\right)} \\ i_{gd-}^{-*}=-\dfrac{s_2 i_{d-}^{-}}{1+s_2} \end{cases} \tag{23}$$

Since the rotor may experience overvoltage or overcurrent during faults, the rotor current reference values should meet the constraints [27] given as:

$$\begin{cases} i_{\mathrm{r\_max}}=\max\left(\sqrt{\left(i_{\mathrm{r}+}^{+}\right)^2+\left(i_{\mathrm{r}-}^{-}\right)^2+2i_{\mathrm{r}+}^{+}i_{\mathrm{r}-}^{-}\cos\left(\delta^{+}-\delta^{-}-\theta^{+}-\theta^{-}\right)}\right) \\ i_{\mathrm{r}+}^{+}=\sqrt{\left(i_{\mathrm{rd}+}^{+}\right)^2+\left(i_{\mathrm{rq}+}^{+}\right)^2} \\ \theta^{+}=\tan^{-1}\left(i_{\mathrm{rq}+}^{+}/i_{\mathrm{rd}+}^{+}\right) \\ i_{\mathrm{r}-}^{-}=\sqrt{\left(i_{\mathrm{rd}-}^{-}\right)^2+\left(i_{\mathrm{rq}-}^{-}\right)^2} \\ \theta^{-}=\tan^{-1}\left(i_{\mathrm{rq}-}^{-}/i_{\mathrm{rd}-}^{-}\right) \end{cases} \tag{24}$$

If the proposed optimal PNS active and reactive currents distribution strategy does not satisfy (25), it further limits the NS voltage components of the rotor during asymmetrical grid faults. To eliminate the NS components in the stator flux and to prevent rotor overvoltage [28], the NS rotor current should be set as:

$$\begin{cases} i_{rd-}^{-*} = -\dfrac{L_m u_{sq-}^{-}}{\sigma L_s L_r \omega_{pll}^{-}} \\ i_{rq-}^{-*} = -\dfrac{L_m u_{sd-}^{-}}{\omega_{pll}^{-} \sigma L_s L_r} \end{cases} \tag{25}$$

where $\sigma = 1 - L_m^2 / L_s L_r$.

Under these conditions, the coordinated distribution strategy of the PNS active and reactive currents between the RSC and GSC should be modified as:

$$\begin{cases} i_{rq+}^{+*} = \dfrac{K^+ \left(0.9 - U_s^+\right) I_N L_s}{L_m \left(1 + s_1\right)} - \dfrac{U_s^+}{L_m \omega_{pll}^+}, \ 0.6 \leqslant U_s^+ \leqslant 0.9 \\ i_{gq+}^{+*} = \dfrac{s_1 K^+ \left(0.9 - U_s^+\right) I_N}{1 + s_1} \\ i_{gd+}^{+*} = k_{dc} \left(U_{dc}^* - U_{dc}\right) \\ i_{rq-}^{-*} = -\dfrac{L_m U_s^-}{\omega_{pll}^- \sigma L_s L_r} \\ i_{gq-}^{-*} = -\dfrac{s_2 U_s^-}{L_s \omega_{pll}^-} \left(1 + \dfrac{L_m^2}{L_r L_s \sigma}\right) \\ i_{rd+}^{+*} = \dfrac{k_{dc} L_s}{s_1 L_m} \left(U_{dc}^* - U_{dc}\right) \\ i_{rd-}^{-*} = 0 \\ i_{gd-}^{-*} = 0 \end{cases} \tag{26}$$

It should be noted that under different asymmetrical grid fault conditions, the corresponding optimal PNS active and reactive currents of the RSC and GSC for the DFIG system can be automatically calculated, provided that the grid fault information required in (19)–(26) is available. Therefore, the proposed strategy is applicable to different types of asymmetrical grid faults. Furthermore, according to the energy equation in (18), the variation boundaries of the DCV can be determined when the equilibrium point of the system does not exist, while under the condition that the equilibrium point of the DFIG system exists, the variation boundaries of the DCV can be obtained using (19). Therefore, the variation boundaries of the DCV for the DFIG system during asymmetrical grid faults can be determined.

V. Simulation and Experiment Validation

A. Simulation Validation

A simulation model is built in MATLAB/Simulink to verify the correctness of the above analysis and the proposed coordinated distribution strategy. Figure 1 illustrates the simulated system configuration, while Table AI in Appendix A provides the detailed parameters of the system, with the transmission line parameters converted to 690 V low-voltage side. Before the occurrence of the fault, the DFIG system operates in MPPT mode, and the DCV is controlled using the PI control strategy. On the AC grid side, a two-phase-to-ground short-circuit fault occurs at 1.6 s. At 1.7 s, the RSC is instantly blocked and adopts a single current loop control strategy. At the same time, the integrator in the DCV control loop is blocked. In Fig. 15, the LVRT current references of the RSC and GSC are assigned according to the values presented in the cases of Table AII in Appendix.

Figure 15 presents the simulation case of the instability phenomenon for the DCV caused by the loss of synchronism of the PNS PLL during angular frequency rise. When U_{fab} decreases to 0.15 p.u., and the current references of the RSC and GSC are set accordingly to Case 1 in Table AII, u_{sq+}^+ and u_{sq-}^- remain greater than 0. Consequently, both P_{do+} and P_{do-} continuously exist, resulting in DC voltage instability. At the same time, as shown in Figs. 15(c) and (f), the output active and reactive power of the DFIG stator and rotor also become unstable.

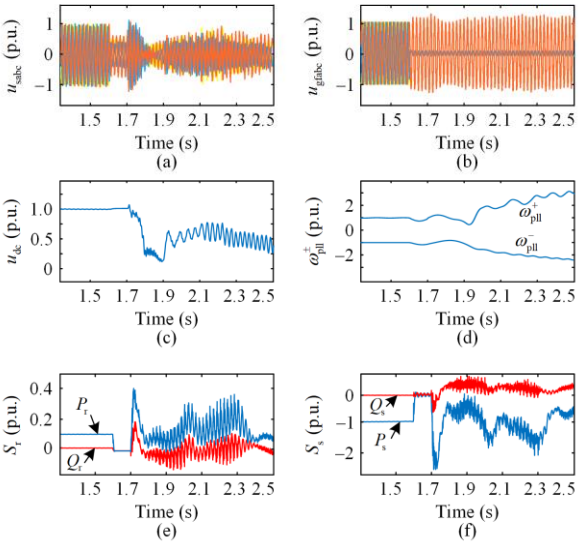

Fig. 15. Case 1: instability of the DCV caused by the lack of an equilibrium point. (a) Three-phase stator voltage of the system. (b) Three-phase fault voltage U_{gfabc}. (c) DCV of the DFIG system. (d) Output frequency of the PNS PLL. (e) Output power of the rotor P_r. (f) Output power of the stator P_s.

Figures 16–18 display the simulation results of the DFIG system when U_{fab} decreases to 0.6 p.u., 0.4 p.u., and 0.2 p.u., respectively. As seen, when the LVRT current references of the RSC and GSC are configured according to Cases 2 to 4 in Table AII, the disturbances of P_{do} and P_{so} can be effectively eliminated using the proposed strategy. As a result, the DCV is rapidly restored to a new stable condition. This demonstrates that the proposed coordinated control strategy can significantly enhance the DCV TS under various levels of grid voltage sags. The simulation outcomes align well with the previous analysis.

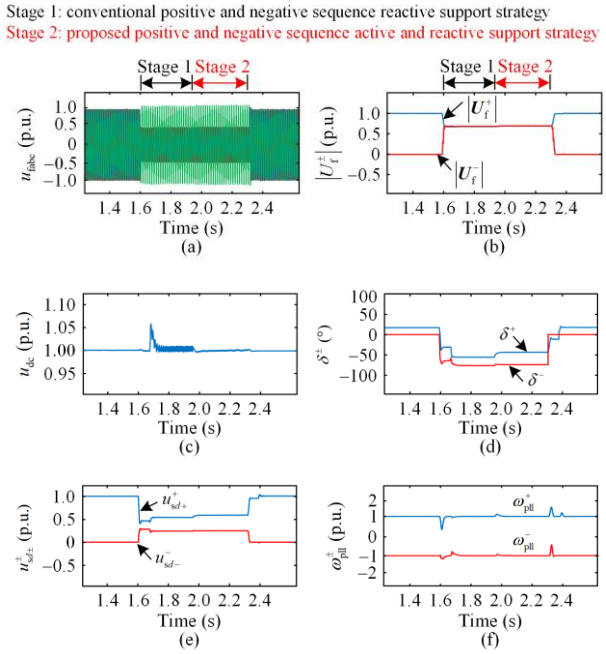

Fig. 16. Case 2: simulation results of the DFIG system when U_{fab} drops to 0.6 p.u. (a) Three-phase voltage of the fault point. (b) Amplitude of the PNS fault voltage. (c) DCV of the DFIG system. (d) PNS equivalent power angles. (e) PNS *d*-axis voltage components. (f) Output frequency of the PNS PLL.

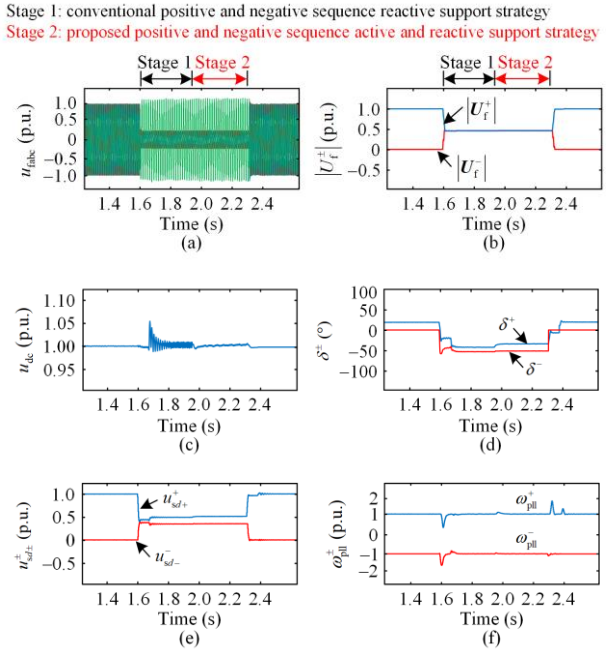

Fig. 17. Case 3: simulation results of the DFIG system when U_{fab} drops to 0.4 p.u. (a) Three-phase voltage at the fault point. (b) Amplitude of the PNS fault voltage. (c) DCV of the DFIG system. (d) PNS equivalent power angles. (e) PNS *d*-axis voltage components. (f) Output frequency of the PNS PLL.

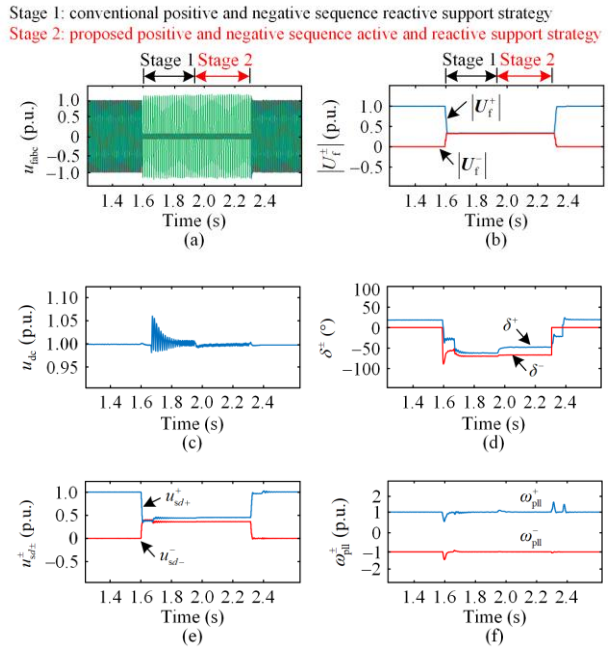

Fig. 18. Case 4: simulation results of the DFIG system when U_{fab} drops to 0.2 p.u. (a) Three-phase voltage at the fault point. (b) Amplitude of the PNS fault voltage. (c) DCV of the DFIG system. (d) PNS equivalent power angles. (e) PNS *d*-axis voltage components. (f) Output frequency of the PNS PLL.

Figure 19 compares the simulation results under different control strategies. When U_{fab} decreases to 0.4 p.u., the DCV deviates from U_{dc0} without applying the proposed strategy during asymmetrical grid faults. Moreover, when the conventional strategy based on PNSC [28] is used, although the DCV can still be controlled to U_{dc0}, both the DCV and the output frequency of the PLL reach the new stable conditions more rapidly with the proposed strategy. In addition, compared with the method in [28], the PNS equivalent power angles remain closer to 0, which applies a greater system TS margin. Therefore, the coordinated current control strategy proposed in this paper can enhance the DCV TS and reduce the risk of transient instability in the DFIG system.

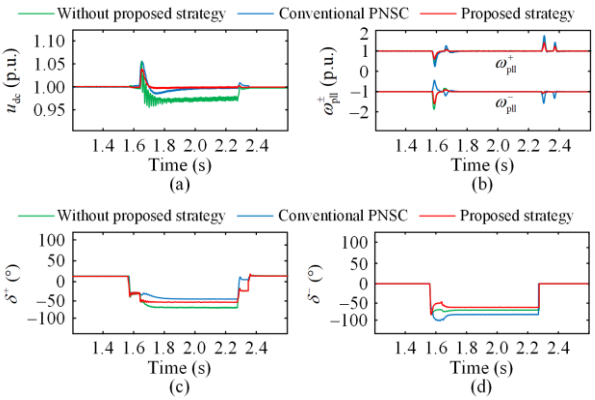

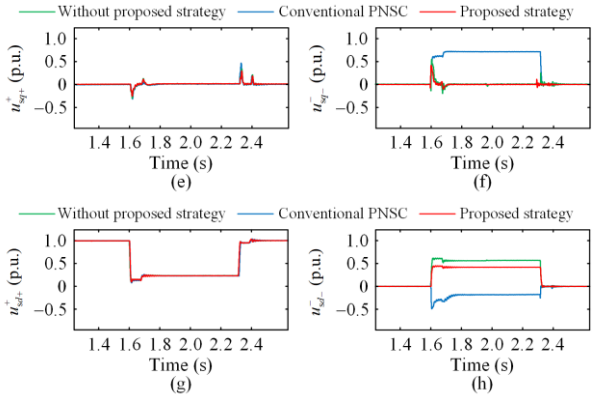

Fig. 19. comparison of simulation results under a two-phase-to-ground fault with different control strategies. (a) DCV of the DFIG system. (b) Output frequency of the PNS PLL (c) PS equivalent power angles. (d) NS equivalent power angles. (e) PS stator voltage $q+$ axis components. (f) NS stator voltage $q-$ axis components. (g) PS stator voltage $d+$ axis components. (h) NS stator voltage $d-$ axis components.

The simulation results of the DCV transient behaviors in the DFIG system under single-line-to-ground fault and phase-to-phase-fault are displayed in Figs. 20 and 21, respectively. The RSC and GSC current references are configured according to Cases 5 and 6 in Table AII. From Figs. 20 and 21, for both asymmetrical faults, the proposed strategy effectively eliminates ΔW_s. Consequently, the DCV is restored to a new stable condition. Therefore, the proposed control strategy effectively improves both the TS level of the DCV and the transient performance of the DFIG system under different types of asymmetrical grid faults.

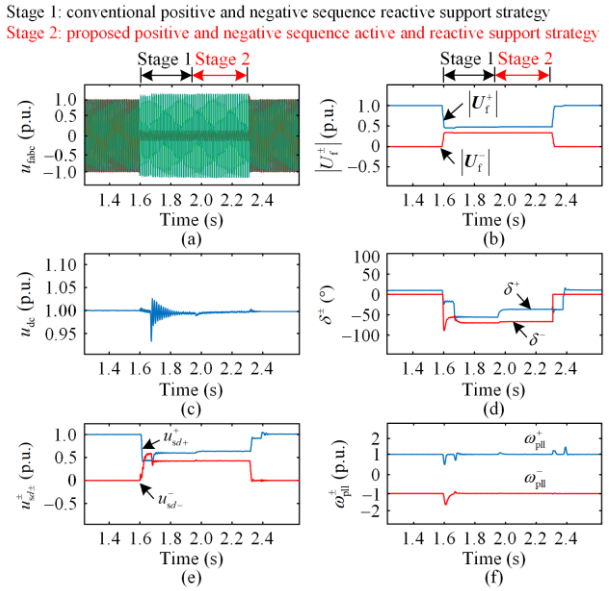

Fig. 20. Case 5: simulation results of the proposed strategy under a single-line-to-ground fault. (a) Three-phase voltage of the fault point. (b) Amplitude of the PNS fault voltage. (c) DCV of the DFIG system. (d) PNS equivalent power angles. (e) PNS *d*-axis voltage components. (f) Output frequency of the PNS PLL.

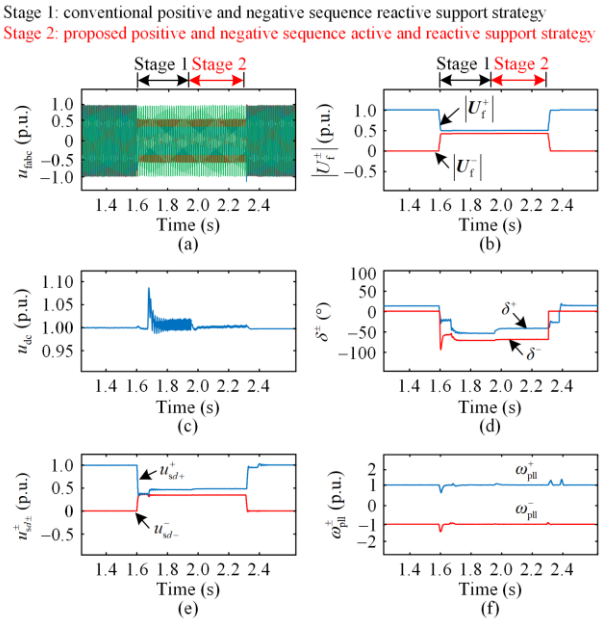

Fig. 21. Case 6: simulation results of the proposed strategy under a phase-to-phase fault. (a) Three-phase voltage of the fault point. (b) Amplitude of the PNS fault voltage. (c) DCV of the DFIG system. (d) PNS equivalent power angles. (e) PNS *d*-axis voltage components. (f) Output frequency of the PNS PLL.

Figure 22 presents the simulation results of the system with the proposed strategy under a three-phase fault. It can be observed that by adjusting the RSC and GSC active and reactive current references in accordance with the control characteristics of the DCV, the DCV can also be effectively regulated to U_{dc0}. Therefore, the control strategy proposed in this work can also be extended to symmetrical grid faults with proper modifications.

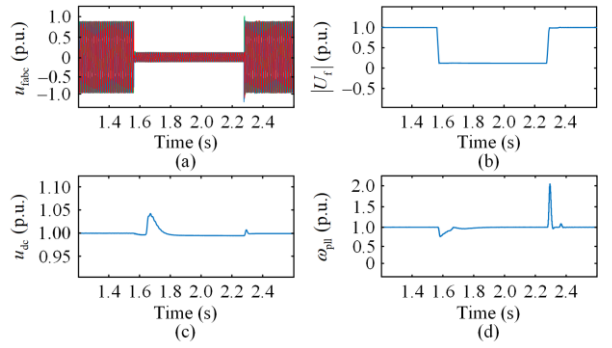

Fig. 22. Simulation results of the proposed strategy under a three-phase fault. (a) Three-phase voltage of the fault point. (b) Amplitude of the fault voltage. (c) DCV of the DFIG system. (d) Output frequency of the PLL.

B. Experimental Validation

Experiments are conducted on a PLL-based DFIG system to further confirm the validity of the theoretical analysis and the proposed strategy. The experimental schematic diagram of the DFIG system is shown in Fig. 23, and Table AIII in Appendix A lists the detailed parameters of the experimental setup. A DC

motor is employed to drive the DFIG system, while the transmission line is simulated using reactors. Data collection is performed using an oscilloscope. Due to the limitation of the experimental setup, only tests under phase-to-phase fault are carried out, implemented using a voltage divider in the AC grid.

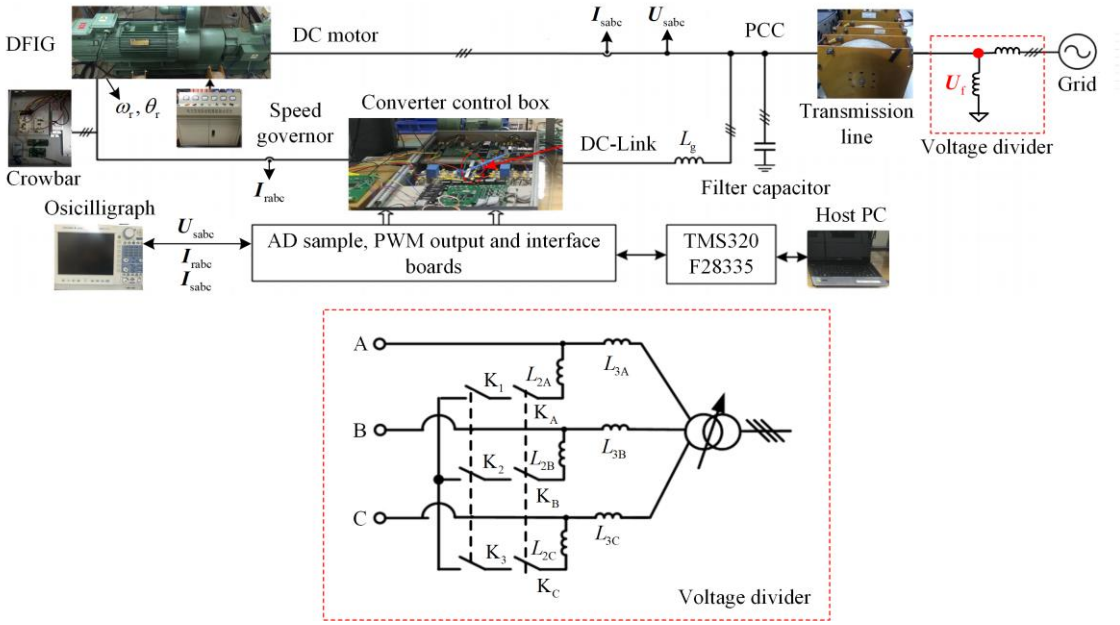

Fig. 23. Experimental detail diagram of the system.

Figure 24 shows the experimental instability results of the DFIG system. The grid fault occurs at 1.5 s, causing U_{fab} to decrease to 0.5 p.u. The RSC is instantly blocked at 1.6 s and adopts the single current loop control strategy. During the fault, the PNS current references of the RSC are set to –0.8 p.u., 0.2 p.u., 0, and 0.3 p.u., while the PNS current references of GSC are set to 0.12 p.u., 0, and 0.1 p.u., respectively. In this case, u_{sq+}^{+} and u_{sq-}^{-} cannot be controlled to 0, and according to (19), the disturbance of P_{do+} and P_{do-} cannot be eliminated. As shown in Fig. 24(b), the DC-link capacitor releases kinetic energy to balance ΔE, leading to transient instability of the DCV. In addition, the output active and reactive power of the DFIG stator and rotor also become unstable, as shown in Figs. 24(d) and (e). These experimental results are consistent with the theoretical analysis.

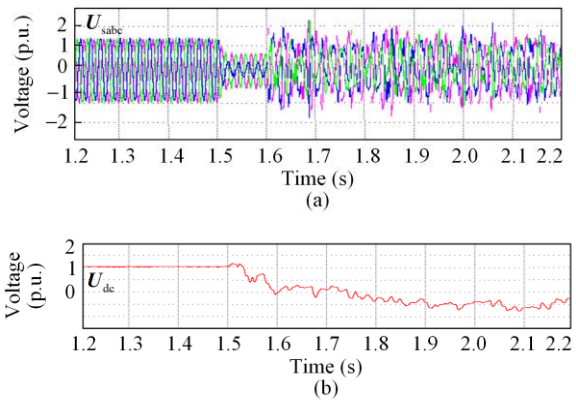

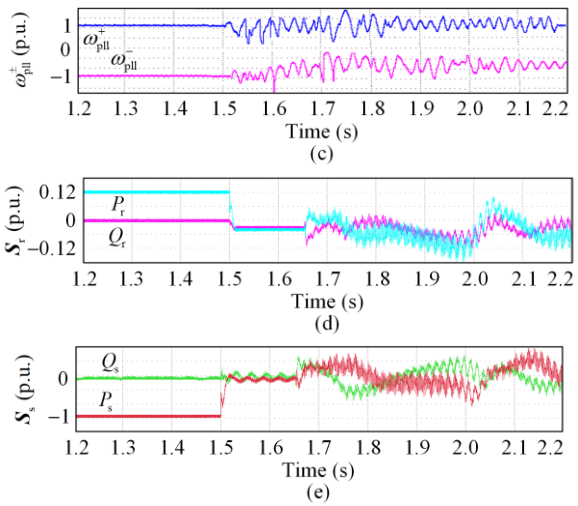

Fig. 24. Instability experimental results of the DFIG system. (a) Three-phase voltage of the DFIG stator. (b) The DC-link capacitor voltage. (c) Output frequency of the PNS PLL. (d) The output active and reactive power of the DFIG rotor. (e) The output active and reactive power of the DFIG stator.

Figures 25(a) and (b) illustrate the experimental results of the DFIG system under a phase-to-phase fault, with and without the application of the proposed control strategy, respectively. In Fig. 25, when U_{fab} decreases to 0.64 p.u. and the PNS active and reactive currents are solely provided by the RSC, as shown in Fig. 25 (a), the DCV diverges from U_{dc0}. By contrast, when the proposed strategy is applied, the disturbance of P_{do} and the imbalance between P_D and P_{so} are completely eliminated. As a result, the DCV is promptly restored to a

new stable state. Moreover, the positive and negative PLLs are also quickly restored to synchronous operation under the proposed method, which indicates that the system has a stronger capability to maintain transient synchronization with the grid during faults. Therefore, the transient response of the DCV and the TS of the DFIG system are effectively improved by the proposed control strategy.

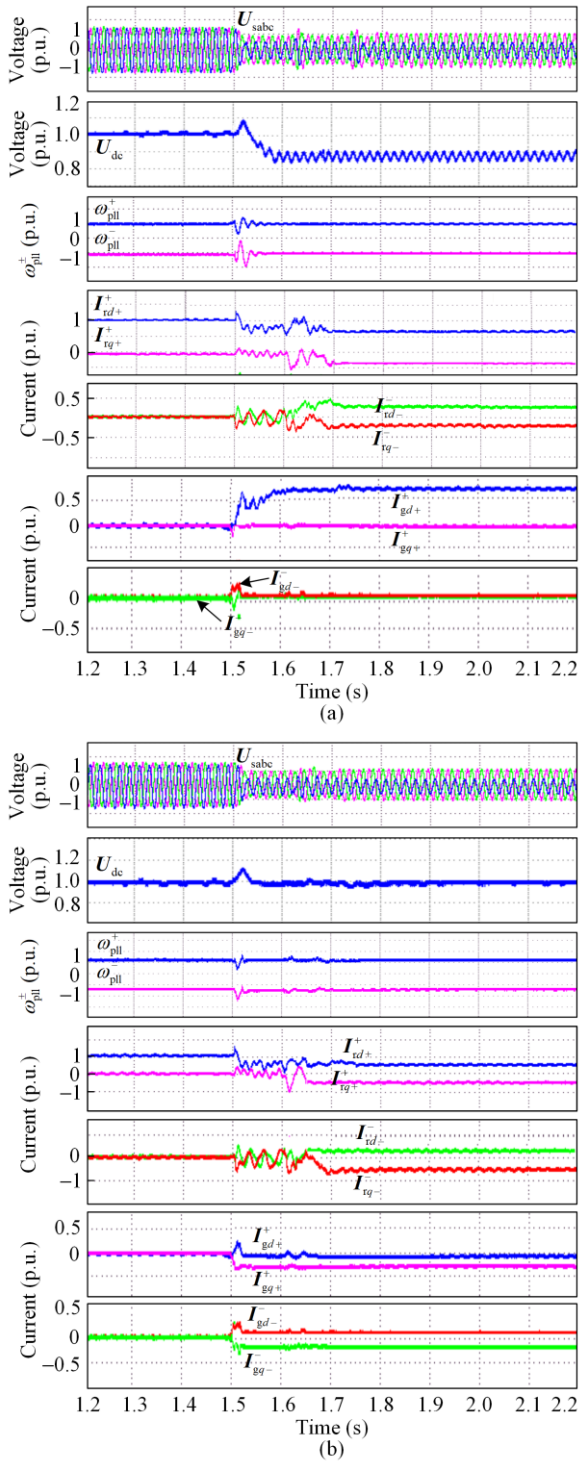

Fig. 25. Experimental comparison of the DFIG system. (a) Results without the proposed method. (b) Results with the proposed method.

VI. Conclusion

This paper thoroughly investigates the transient behavior and stability control strategy of DCV in PLL-based DFIG systems during asymmetrical grid faults. The findings can effectively prevent wind farms from disconnecting from the grid and avoid large-scale economic losses. The conclusions are summarized as follows.

1) Based on the dual-sequence synchronization nonlinear transient model, the equivalent damping power, the equivalent static stable power, and the equivalent dynamic stable power are the key factors that affect the transient behavior of the DCV. These components are influenced by the control characteristics of the PNS PLL and by the power coordination between the RSC and GSC.

2) The impact of different parameters on the DCV TS is analyzed, and the TS process of the DCV under asymmetrical grid faults is described. The findings show that if dynamic stable power cannot be eliminated, the DCV will exhibit different instability phenomena. Furthermore, when the imbalance between the static stable power and damping power cannot be mitigated, the DCV will display different levels of TS during asymmetrical faults. Therefore, the influence of the transient behavior among converters on the TS of smart grids with high renewable energy penetration cannot be overlooked, and it should be considered when designing LVRT control strategies.

3) A control strategy is introduced to enhance the TS of the DCV during asymmetrical grid faults. Through the coordination of the LVRT current references of the RSC and GSC, the strategy effectively improves the TS level of the DCV under such faults. It should be noted that the effectiveness of this approach relies on the rapid acquisition of fault information, and further investigation is needed on how to obtain this information promptly in a real-world grid-connected DFIG systems.

Appendix A

A. Simulation Parameters

TABLE AI
Parameters of the Simulation DFIG System

Symbol	Description	Value
S_N (MW)	Rated power	200
U_N (V/kV)	Rated voltage	690/35/220
U_{dc} (V)	DC-link voltage	1200
R_s, L_s (p.u.)	Stator resistance and inductance	0.0189, 2.68
R_r, L_r (p.u.)	Rotor resistance and inductance	0.016, 2.54
Z_f (p.u.)	Fault impedance	0.009
p	Pole pair	2
C (μF)	DC-link capacitor	18
L_m (mH)	Mutual inductance	16.5
$Z^+_L = Z^-_L$ (p.u.)	Line impedance	0.059+j0.963
Z^0_L (p.u.)	Line zero sequence impedance	0.123+j0.899
Z_{L_f} (p.u.)	Phase-phase impedance	0.0397

B. Current References

TABLE AII
CURRENT REFERENCES OF SIMULATION CASES

(p.u.)

Case	i_{rd+}^{+*}	i_{rq+}^{+*}	i_{rd-}^{-*}	i_{rq-}^{-*}	i_{gd+}^{+*}	i_{gd-}^{-*}	i_{gq-}^{-*}
1	0.95	−0.2	0	−0.15	0.2	0	0
2	0.35	−0.31	0.15	−0.35	0.12	−0.1	0.11
3	0.23	−0.38	0.11	−0.42	0.22	−0.07	0.21
4	0.12	−0.45	0.05	−0.43	0.28	−0.05	0.25
5	0.25	−0.36	0.12	−0.39	0.21	−0.09	0.18
6	0.39	−0.14	0.18	−0.27	0.13	−0.13	0.15

C. Experimental Parameters

TABLE AIII
PARAMETERS OF THE EXPERIMENTAL DFIG SYSTEM

Symbol	Description	Value
S_N (kW)	Rated power	1.5 (1 p.u.)
U_N (V)	Rated voltage	220 (1 p.u.)
U_{dc} (V)	DC-link voltage	400 (1 p.u.)
f_n (Hz)	Frequency	50 (1 p.u.)
L_s (mH), R_s (Ω)	Stator inductance and resistance	66.6, 1.09
L_m (mH)	Mutual inductance	64.6
L_r(mH), R_r (Ω)	Rotor inductance and resistance	66.6, 1.5
L (mH), R (Ω)	Transmission line inductance and resistance	21, 1.5
C (μF)	DC-link capacitor	30
p	Pole pair	2
$k_{p\_pll\_faut}^{+}$, $k_{i\_pll\_faut}^{+}$	PI gains of the positive PLL	0.04, 0.005
$k_{p\_pll\_faut}^{-}$, $k_{i\_pll\_faut\_}^{-}$	PI gains of the negative PLL	0.065, 0.015

ACKNOWLEDGMENT

Not applicable.

AUTHORS' CONTRIBUTIONS

Yi Luo: modeling the system, designing the algorithm of control strategy, and writing the paper. Jun Yao: putting forward the initial concept and giving technical guidance in the whole process. Dong Yang: checking the data and experimental results. Hai Xie: demonstrating the strategy proposed in the paper. Linsheng Zhao: giving technical guidance in the whole process. Rongyu Jin: typesetting the manuscript. All authors read and approved the final manuscript.

FUNDING

This work is supported in part by Smart Grid-National Science and Technology Major Project (No. 2024ZD0801400), and Science and technology projects of State Grid Corporation of China (No. 52272224000V).

AVAILABILITY OF DATA AND MATERIALS

Not applicable.

DECLARATIONS

Competing interests: The authors declare that they have no known competing financial interests or personal relationships that could have appeared to influence the work reported in this article.

AUTHORS' INFORMATION

Yi Luo received the B.Eng. degree in electrical engineering and automation from Soochow University, Suzhou, China in 2020. He is currently working toward the Ph.D. degree in electrical engineering with the School of Electrical Engineering at Chongqing University. His research interests include electric machines control, modeling and control of wind turbine generation system, and renewable power generation.

Jun Yao received the B.Eng., M.Sc., and Ph.D. degrees from Chongqing University, Chongqing, China, in 2001, 2004, and 2007, respectively, all in electrical engineering. Since 2004, he has been with the School of Electrical Engineering, Chongqing University, where he is currently a professor. He was a visiting researcher with the Department of Energy Technology, Aalborg University, Aalborg, Denmark, from January 2012 to January 2013. He is a member of IEC TC 8/SC 8A/JWG 5. He has authored or coauthored more than 100 peer-reviewed technical papers, and holds more than 20 issued/pending patents. His research interests include electric machines control, power electronics conversion and control, and renewable power generation, and his main current research interests include wind energy and power electronics application to the power systems.

Dong Yang received the B.Eng. degree in electrical engineering and automation from Yanshan University, Qinhuangdao, China, in 2022. He is currently working toward the Ph.D. degree with the School of Electrical Engineering, Chongqing University, Chongqing, China. His research interests include control of stability of power system and renewable power generation.

Hai Xie received the B.Eng. degree in electrical engineering and automation from Taiyuan University of Technology, Taiyuan, China, in 2022. He is currently working toward the M.S. degree in electrical engineering with the School of Electrical Engineering, Chongqing University, Chongqing, China. His research interests include large-disturbance stability analysis of wind energy conversion system and grid-forming control.

Linsheng Zhao received the B.Eng. degree in electrical engineering and automation from Anhui University, Hefei, China, in 2023. He is currently working toward the Ph.D. degree in electrical engineering with the School of Electrical Engineering, Chongqing University, Chongqing, China. His research interests include influence of wind power integration on stability of power system, and control of wind turbine generation system.

Rongyu Jin received the B.Eng. degree in electrical engineering from Chongqing University, Chongqing, China, in 2023. He is currently working toward the M.Sc. degree in electrical engineering with the School of Electrical Engineering, Chongqing University, Chongqing, China. His research interests include transient stability of renewable power generation system, protection, and control of wind farms with MMC-HVDC transmission system.

REFERENCES

[1] H. Wu, H. Xu, and Z. Li *et al.*, "Reactive current distribution strategy of DFIG's RSC and GSC considering electromagnetic stress and grid codes requirement," *IEEE Transactions on Energy Conversion*, vol. 38, no. 1, pp. 273-283, Mar. 2023.

[2] A. Khan, M. Hosseinzadehtaher, and M. B. Shadmand *et al.*, "On the stability of the power electronics-dominated grid: A new energy paradigm," *IEEE Transactions on Power Electronics*, vol. 14, no. 4, pp. 65-78, Dec. 2020.

[3] H. Xu, J. Hu, and Y. He, ''Operation of wind-turbine-driven DFIG systems under distorted grid voltage conditions: analysis and experimental validations,'' *IEEE Transactions on Power Electronics*, vol. 27, no. 5, pp. 2354-2366, May 2012.

[4] National Grid ESO., "Interim report into the low frequency demand disconnection (LFDD) following generator trips and frequency excursion on 9 Aug 2019," National Grid ESO., UK, 2019.

[5] H. Yuan, H. Xin, and L. Huang *et al.*, "Stability analysis and enhancement of type-4 wind turbines connected to very weak grids under severe voltage sags," *IEEE Transactions on Energy Conversion*, vol. 34, no. 2, pp. 838-848, Jun. 2019.

[6] J. Pei, J. Yao, and Y. Liu, *et al.*, "Modeling and transient synchronization stability analysis for PLL-based renewable energy generator considering sequential switching schemes," *IEEE Transactions on Power Electronics*, vol. 37, no. 2, pp. 2165-2179, Feb. 2022.

[7] M. Edrah, K. L. Lo, and O. Anaya-Lara, "Impacts of high penetration of DFIG wind turbines on rotor angle stability of power systems," *IEEE Transactions on Sustainable Energy*, vol. 6, no. 3, pp. 759-766, Jul. 2015.

[8] L. Xu and Y. Wang, "Dynamic modeling and control of DFIG-based wind turbines under unbalanced network conditions," *IEEE Transactions on Power Systems*, vol. 22, no. 1, pp. 314-323, Feb. 2007.

[9] A. M. Eltamaly, M. S. Al-Saud, and A. G. Abo-Khalil, "Dynamic control of a DFIG wind power generation system to mitigate unbalanced grid voltage," *IEEE Access*, vol. 8, pp. 39091-39103, Feb. 2020.

[10] L. Xiong, F. Zhou, and F. Wang *et al.*, "Static synchronous generator model: a new perspective to investigate dynamic characteristics and stability issues of grid-tied PWM inverter," *IEEE Transactions on Power Electronics*, vol. 31, no. 9, pp. 6264-6280, Sept. 2016.

[11] S. Chen, J. Yao, and J. Pei *et al.*, "Transient stability analysis and improved control strategy for DC-link voltage of DFIG-based WT during LVRT," *IEEE Transactions on Energy Conversion*, vol. 37, no. 2, pp. 880-891, Jun. 2022.

[12] H. Yuan, X. Yuan, and J. Hu, "Modeling of grid-connected VSCs for power system small-signal stability analysis in DC-link voltage control timescale," *IEEE Transactions on Power Systems*, vol. 32, no. 5, pp. 3981-3991, Sept. 2017.

[13] J. Hu, H. Yuan, and X. Yuan. "Modeling of DFIG-based WTs for small-signal stability analysis in DVC timescale in power electricized power systems," *IEEE Transactions on Energy Conversion*, vol. 32, no. 3, pp. 1151-1165, Sept. 2017.

[14] Ö. Göksu, R. Teodorescu, and C. L. Bak *et al.*, "Impact of wind power plant reactive current injection during asymmetrical grid faults," *IET Renewable Power Generation,* vol. 7, no. 5, pp. 484-492, Sept. 2013.

[15] R. Liu, J. Yao, and P. Sun *et al.* "Complex impedance-based frequency coupling characteristics analysis of DFIG-based WT during asymmetric grid faults," *IEEE Transactions on Industrial Electronics*, vol. 68, no. 9, pp. 8274-8288, Sept. 2021.

[16] Y. Luo, J. Yao, and Z. Chen *et al.*, "Transient synchronous stability analysis and enhancement control strategy of a PLL-based VSC system during asymmetric grid faults," *Protection and Control of Modern Power Systems*, vol. 8, no. 2, pp. 1-17, Mar. 2023.

[17] G. Ding, F. Gao, and H. Hao *et al.*, "Adaptive DC-link voltage control of two-stage photovoltaic inverter during low voltage ride-through operation," *IEEE Transactions on Power Electronics*, vol. 31, no. 6, pp. 4182-4194, Jun. 2016.

[18] R. A. J. Amalorpavaraj, P. Kaliannan, and S. Padmanaban *et al*., "Improved fault ride through capability in DFIG based wind turbines using dynamic voltage restorer with combined feed-forward and feed-back control," *IEEE Access*, vol. 5, pp. 20494-20503, Sept. 2017.

[19] H. Wang, J. Zhang, and C. Zhu *et al*., "DC-link current optimal control of current source converter in DFIG," *CPSS Transactions on Power Electronics and Applications*, vol. 6, no. 2, pp. 127-135, Jun. 2021.

[20] J. Lu, S. Golestan, and M. Savaghebi *et al*., "An enhanced state observer for DC-link voltage control of three-phase AC/DC converters," *IEEE Transactions on Power Electronics*, vol. 33, no. 2, pp. 936-942, Feb. 2018.

[21] Y. Tian, P. C. Loh, and F. Deng *et al*., "DC-link voltage coordinated-proportional control for cascaded converter with zero steady state error and reduced system type," *IEEE Transactions on Power Electronics*, vol. 31, no. 4, pp. 3177-3188, Apr. 2016.

[22] Technical Regulations for Connecting Wind Farms to Electric Power Systems—Part 1: Onshore Wind Power, Chinese Standard GB/T 19963.1-2021, 2021.

[23] Technical Requirements for the Connection and Operation of Customer Installations to the High Voltage Network for Germany, VDE-AR-N 4120, 2015.

[24] IEEE Standard for Interconnection and Interoperability of Inverter-based Resources (IBRs) Interconnecting with Associated Transmission Electric Power Systems, IEEE standard 2800-2022, 2022.

[25] T. Wang and H. Nian, "Flexible PCC voltage unbalance compensation strategy for autonomous operation of parallel DFIGs," in *2016 IEEE Energy Conversion Congress and Exposition (ECCE)*, Milwaukee, USA, Feb. 2017, pp. 4807-4820.

[26] X. He, C. He, and S. Pan *et al*., "Synchronization instability of inverter-based generation during asymmetrical grid faults," *IEEE Transactions on Power Systems*, vol. 37, no. 2, pp. 1018-1031, Mar. 2022.

[27] H. Xu, Y. Zhang, and Z. Li *et al*., "Reactive current constraints and coordinated control of DFIG's RSC and GSC during asymmetric grid condition," *IEEE Access*, vol. 8, pp. 184339-184349, Oct. 2020.

[28] A. A. Montanari and A. M. Gole, "Enhanced instantaneous power theory for control of grid connected voltage sourced converters under unbalanced conditions," *IEEE Transactions on Power Electronics*, vol. 32, no. 8, pp. 6652-6660, Aug. 2017.